



Matjuschkin, V., Blundy, J. D., & Brooker, R. A. (2016). The effect of pressure on sulphur speciation in mid to deepcrustal arc magmas and implications for the formation of porphyry copper deposits. *Contributions to Minerology and Petrology*, 171, [66]. DOI: 10.1007/s00410-016-1274-4

Peer reviewed version

Link to published version (if available):
[10.1007/s00410-016-1274-4](https://doi.org/10.1007/s00410-016-1274-4)

[Link to publication record in Explore Bristol Research](#)
PDF-document

This is the author accepted manuscript (AAM). The final published version (version of record) is available online via Springer at <http://link.springer.com/article/10.1007/s00410-016-1274-4>. Please refer to any applicable terms of use of the publisher.

University of Bristol - Explore Bristol Research

General rights

This document is made available in accordance with publisher policies. Please cite only the published version using the reference above. Full terms of use are available:
<http://www.bristol.ac.uk/pure/about/ebr-terms.html>

The effect of pressure on sulphur speciation in mid- to deep-crustal arc magmas and implications for the formation of porphyry copper deposits

Vladimir Matjuschkin^{1*}, Jon D. Blundy¹ and Richard A. Brooker¹

School of Earth Sciences, University of Bristol, Wills Memorial Building, Queens Road, Bristol BS8 1RJ, United Kingdom

* vladimir.matjuschkin@bristol.ac.uk
vladimirgeo@googlemail.com

Abstract

Piston cylinder experiments are used to investigate the effect of oxygen fugacity (fO_2) on sulphur speciation and phase relations in arc magmas at 0.5 to 1.5 GPa and 840-950°C. The experimental starting composition is a synthetic trachyandesite containing 6.0 wt% H₂O, 2880 ppm S, 1500 ppm Cl and 3880 ppm C. Redox conditions ranging from 1.7 log units below the Ni-NiO buffer (NNO-1.7) to NNO+4.7 were imposed by solid state buffers: Co-CoO, Ni-NiO, Re-ReO₂ and Hematite-Magnetite. All experiments are saturated with a COH-fluid. Experiments produced crystal-bearing trachydacitic melts (SiO₂ from 60 to 69 wt%) for which major and volatile element concentrations were measured. Experimental results demonstrate a powerful effect of oxidation state on phase relations. For example, plagioclase was stable above NNO, but absent at more reduced conditions. Suppression of plagioclase stability produces higher Al₂O₃ and CaO melts. The solid sulphur-bearing phases and sulphur speciation in the melt are strong functions of fO_2 , as expected, but also of pressure. At 0.5 GPa the anhydrite stability field is intersected at NNO \geq +2, but at 1.0 and 1.5 GPa experiments at the same fO_2 produce sulphides and the stability field of sulphate moves towards higher fO_2 by \sim 1 log unit at 1.0 GPa and \sim 1.5 log units at 1.5 GPa. As a result, models that appeal to high oxidation state as an important control on the mobility of Cu (and other chalcophiles) during crustal differentiation must also consider the enhanced stability of sulphide in deep- to mid-crustal cumulates even for relatively oxidised (NNO+2) magmas. Experimental glasses reproduce the commonly observed minimum in sulphur solubility between the S²⁻ and S⁶⁺ stability fields. The solubility minimum is not related to the Fe content

(Fe²⁺/Fe³⁺ or total) of the melt. Instead we propose this minimum results from an unidentified, but relatively insoluble, S species of intermediate oxidation state.

Keywords: sulphur solubility and speciation, oxygen fugacity, phase relations, hydrous magma, porphyry copper deposit

1. Introduction

The vast majority of porphyry copper deposits (PCDs) form in metallogenic belts sub-parallel to subduction-related volcanic arcs (e.g. Camus and Dilles 2001; Sillitoe 2012). As a result, there has been considerable speculation that their origin might be a consequence of the oxidized nature of arc magmas and/or the sub-arc mantle environment (see Fig. 1a), possibly influenced by the increased stability of sulphate relative to sulphides (e.g. Mungall 2002; Jugo 2009; Sato 2012). Copper itself is much less sensitive to variable oxidation state and is monovalent for most magmatic conditions (Candela and Holland 1984). However, copper is considered a chalcophile element¹ and can form solid sulphide phases or partition strongly into immiscible sulphide liquids. As sulphur is multivalent, its speciation is strongly controlled by the oxidation state of magma, often expressed in terms of the oxygen fugacity (fO_2). At reduced conditions Fe-sulphide saturation during magmatic differentiation sequesters copper into a sulphide-bearing cumulate assemblages, depleting the evolved silicate melts in copper. At more oxidized conditions, calcium sulphate (anhydrite) forms instead of sulphides. Copper does not partition into anhydrite, consequently in oxidised systems copper behaves as an incompatible element during differentiation, becoming enriched in the evolving silicate melt.

Previous experimental studies on basalts at 200 MPa (Jugo et al. 2010; Botcharnikov et al. 2010) suggest that the transition from sulphide to sulphate stability (and S²⁻ to SO₄²⁻ species in the melt) occurs as fO_2 is increased from the nickel-nickel oxide buffer (NNO) to 1.5 log units above, such that sulphate is the only stable S-species at $fO_2 > NNO+1.5$ (Fig. 1b). This is at the high end of the fO_2 range observed in most basalts erupted at the Earth's surface, but within the range of arc magmas (Figure 1a). At a given pressure, the fO_2 of the sulphide-sulphate transition has been shown

¹ Technically chalcophile means “copper-loving”, although it is widely used to indicate a “sulphur-loving” (thiophile) element and that is the meaning intended here

to increase slightly with increasing silica (by ~ 0.1 log units) for a trachyandesite and by a further 0.5 log units for rhyolite (Massota and Keppler 2015), although Carroll and Rutherford (1987) report anhydrite stability by $\text{NNO}+0.8$ for a trachyandesite. It has also been established that oxidized conditions produce a sulphate solubility (S^{6+} species in the melt) that is 2-5 times higher compared to the sulphide solubility (S^{2-} species in the melt) prevalent at reduced condition (e.g. Carroll and Rutherford 1987; Luhr 1990; Massota and Keppler 2015). The higher sulphur solubility and the inhibition of dense sulphide precipitation implies that high oxidation state can promote both S and Cu enrichment in evolving silicate melts favouring the eventual formation of porphyry copper deposits (e.g. Mungall 2002; Sun et al. 2013).

One main line of evidence that arc magmas are on average more oxidised than those produced at mid-ocean ridges or in other settings (Fig. 1a) is based on a comparison of Fe^{3+} and Fe^{2+} ratios in lavas erupted at the Earth's surface (e.g. Carmichael 1991; Ballhaus 1993; Kelley and Cottrell 2009; Lee et al. 2010, Foley 2011). This is further supported by the occurrence of anhydrite in many oxidized, erupted arc magma such as Pinatubo, Philippines (Bernard et al. 1991) or El Chichón, Mexico (Luhr, 1990). However, there is considerable debate regarding the mechanism that produces these oxidized conditions (e.g. Kelley and Cottrell 2009, 2012; Humphreys et al. 2015). It has long been believed that the transfer of hydrous fluids (\pm sulphur) from the 'oxidized' subducting slab was the primary cause and the addition of this fluid to the mantle wedge must lead to a higher $f\text{O}_2$ for the sub-arc mantle compared with more 'normal' mantle that is the source of MOR basalts (Evans et al. 2012; Crabtree and Lange 2012). This view is supported by comparison between mantle xenoliths from the various tectonic environments, also shown in Fig. 1a (Wood et al. 1990; Brandon and Draper 1992; Johnson et al. 1996; Parkinson and Arculus 1999). However, an alternate view has been put forward recently based on redox-sensitive element partitioning or isotope fractionations that are inconsistent with melt generation from an oxidized, sub-arc mantle source (see Fig. 1a; Dauphas et al. 2009; Lee et al. 2005; 2010; Mallmann and O'Neill 2009). The proponents of this view reason that arc magmas must acquire their oxidized character en route from their mantle source to the Earth's surface. In particular they appeal to major differences in magmatic processes and timescales between dry MORB and volatile-rich arc systems.

As noted by Humphreys et al. (2015) an intriguing point in support of a change in oxidation state during crustal processes is the occurrence of Cu-Fe-sulphide inclusions in early-stage phenocrysts (or 'antecrysts') that are found in magmas erupted with an oxidation state apparently too high to stabilize sulphide phases (e.g. Shiveluch Volcano, Kamchatka, Humphreys et al. 2006; Santiaguito, Guatemala, Scott et al. 2013; Satsuma-Iwojima, Japan, Ueda and Itaya 1981; and Popocatépetl, Mexico, Schaaf et al. 2005), and sometimes also in the associated cumulates (Lee et al. 2012). This even seems to be true for Mount Pinatubo, where sulphate is clearly the stable sulphur-bearing phase in the final erupted magma (Pallister et al. 1996; Hattori 1993). Humphreys et al. (2015) suggest this behavior might be related to a change in water activity ($a_{\text{H}_2\text{O}}$), but note that magnetite crystallisation has been proposed as an alternative option (Carmichael and Ghiorso 1986; Sun et al. 2004; Jenner et al. 2010), leading to a complex interplay between $\text{Fe}^{3+}/\text{Fe}^{2+}$ and $\text{S}^{6+}/\text{S}^{2-}$ ratios in the melt (Sun et al. 2004; Moretti and Papale 2004). Unfortunately, our understanding of the relationship between $f\text{O}_2$ and sulphur oxidation state is limited to relatively shallow conditions (<500 MPa) making interpretation of any early, deeper differentiation processes very difficult.

The aim of this study is to explore the behaviour of sulphur at high-pressure conditions representing lower to middle crustal magmatic processes. We use experiments performed in piston cylinder apparatus and $f\text{O}_2$ conditions imposed by solid-state buffers (Fig. 1b); Cobalt-Cobalt Oxide (Co-CoO), Nickel-Nickel Oxide (NNO), Rhenium-Rhenium Oxide (Re-ReO₂), and, Haematite-Magnetite (H-M or Fe₂O₃-Fe₃O₄). In particular we determine the $f\text{O}_2$ required to transition from the sulphide-dominated to the sulphate-only stability fields at pressures up to 1.5 GPa, by varying the $f\text{O}_2$ from NNO-1.5 to NNO+2 and in some cases up to NNO +4.7. This encompasses almost the entire $f\text{O}_2$ range of subduction zone magmas (Fig 1a). The influence of deep crustal sulphur speciation on Cu mobility and subsequent PCD formation is assessed. In addition we present some basic textural observations, phase relations and melt composition for each $f\text{O}_2$ investigated, to identify differences between oxidized and reduced fractionation trends in hydrous arc magmas.

2. Experimental methodology

2.1 Starting composition

The starting composition (Table 1) was prepared from various synthetic materials (albite, anorthite, orthoclase, fayalite, quartz, rutile and hematite). Its chemistry (on an a volatile-free basis) approximates that of aphyric basaltic trachyandesite 'FM37' (Frey et al. 1984) from Laguna del Maule, an active volcanic caldera complex on the Chile-Argentina boarder in the Andean Southern Volcanic Zone. The ratio of fayalite (Fe^{2+}) to hematite (Fe^{3+}), was used to fix the $\text{Fe}^{3+}/\sum\text{Fe}$ of the starting mix at ~ 0.3 corresponding to $\Delta\text{NNO} \approx +1.2$ at 200 MPa and 1000 °C (Carmichael 1991). The starting mix was doped with 1500 ppm Cl added as NaCl and 2880 ppm S, one half of which was added as FeS (S^{2-}) and the other as $\text{CaSO}_4 \cdot 2\text{H}_2\text{O}$ (S^{6+}). In addition, 3800 ppm carbon was added as CaCO_3 by controlled reaction of $\text{Ca}(\text{OH})_2$ with CO_2 in air. This amount of carbon is at the high end of concentrations expected for arc magmas (see Lowenstern 2001; Blundy et al. 2010), but was designed to ensure excess fluid was present in all runs (see Results). Final concentrations of carbon and sulphur in the starting mix were determined using an ELTRA CS800 analyser at Leibniz Universität Hannover. In order to examine the homogeneity of S and C, three different batches of starting material were analysed; the concentrations are identical within the measurement uncertainty (± 30 ppm). Water contents of 6 wt.% were added as hydroxides $\text{Mg}(\text{OH})_2$, $\text{Al}(\text{OH})_3$, $\text{Ca}(\text{OH})_2$. Batches of 10-20 capsules were prepared at one time, whilst the remaining material was stored in a sealed glass vial to prevent further reaction with atmospheric CO_2 .

2.2 Experimental set-up

High-pressure experiments were carried out in an end-loaded piston cylinder apparatus at University of Bristol. Runs at 1.0 and 1.5 GPa were performed using a 12.5 mm salt-Pyrex assembly, whilst the run at 0.5 GPa (nominal) used a 19 mm "Kushiro" talc-Pyrex assembly (see McDade et al. 2002). Capsule configuration followed the design of Matjuschkin et al. (2015) to maintain the required $f\text{O}_2$. Information about quench-rate, attainment and maintenance of $f\text{O}_2$ equilibrium and its high accuracy and precision, as well as detailed sketches of the experimental setup are provided in Matjuschkin et al. (2015). The triple capsule assembly consists of (i) an outer 10 mm-long gold outer capsule ($\varnothing=3$ mm) containing crushable alumina powder and 6 μl H_2O , (ii) an inner 5 mm-long platinum capsule ($\varnothing = 2$ mm)

containing solid redox buffer and 3 μl H_2O and (iii) an inner 3mm-long gold capsule ($\varnothing = 2$ mm) containing 5 mg of starting material. The reason for such a small amount of starting material was to ensure early achievement of $f\text{O}_2$ equilibrium between the buffer and the sample (see Matjuschkin et al. 2015, experiment MTB/RR0-24L). All capsules were pre-annealed at 1000°C for about 1 hour, then loaded with the relevant material, wrapped in a wet paper tissue, cooled with freezer spray and welded shut using a micro-spot welder. Finally, this capsule assembly was checked for water leakage by weighing before and after storing in a 200 °C drying oven. The capsule assembly was placed into a solid Pyrex sleeve, with any space filled with Pyrex powder and $\varnothing = 3$ mm, 0.1 mm-thick solid Pyrex discs were placed at both ends. Pyrex is used in order to minimize both hydrogen exchange with the pressure cell and carbon infiltration from the furnace (Brooker et al. 1998; Matjuschkin et al. 2015). Experiments were carried out at 0.5, 1 and 1.5 GPa and temperatures from 840-950 °C. Further experiments at temperatures $>975^\circ$ all failed, probably as a result of the formation of an immiscible sulphide melt that attacks the capsule material, unlike at lower temperature where a solid sulphide phase forms. The resulting loss of sulphur in failed experiments produced a strong H_2S smell when opening the outer Au capsule. Further attempts to run experiments replacing Au with AuPd capsules failed due to formation of PdS, which removes almost the entire sulphur content of the experiment within <1 hour (even shorter than the <6 hr reported by Jugo et al. 2005). It appears unlikely that shorter runs would reach equilibrium, especially using our particular solid-state buffer technique.

Our approach was to control the redox state of each experimental charge by using the different solid redox buffers described above (Fig. 1b). Buffer materials were placed into Pt capsules in proportion 1 mol metal to 1 mol metal oxide, with the exception of the most reduced Co-CoO buffered experiments, where the decision to use only Co metal was justified by relative high $f\text{O}_2$ difference between the starting material and buffer itself. Pt is used for its high melting point and its high H_2 permeability allowing the buffer to rapidly impose the required $f\text{O}_2$ (more correctly, the $f\text{H}_2$).

Experimental temperatures were monitored with type D $\text{W}_3\text{Re}_{97}\text{-W}_{25}\text{Re}_{75}$ thermocouples. These thermocouples showed evidence of oxidation in the HM experiments leading to erroneous temperatures. For those runs the temperature was

controlled by the power output alone. The actual temperature of these experiments was cross-checked using the hornblende-plagioclase thermometer of Holland and Blundy (1994) applied to the run products.

Pressure was controlled automatically within of ± 3 MPa of the set point and a 3% friction correction was applied following McDade et al. (2002) for the 12.5 mm assembly (1.0 and 1.5 GPa). The 19 mm assembly is not calibrated at 0.5 GPa and although there is no correction required at 1.0 GPa (McDade et al. 2002) it is likely the true pressure was as low as 0.43 GPa (see below), so the quoted 0.5 GPa is 'nominal'. Run durations were ~ 4 days. Experiments were quenched by cutting-off power to the furnace. Recovered capsule assemblies were embedded in epoxy resin, pierced with a sharp blade to ensure the presence of water in the outer and inner capsules, then ground with silicon carbide and finally polished, all using oil rather than water-based lubricants to prevent dissolution of any run-product sulphate minerals. Redox buffers were examined and only runs with both metal and metal oxide components present at the conclusion of the run are reported here.

2.3 Fluid composition and experimental redox conditions

In our experiments the fO_2 of the sample is only equal to the fO_2 of the buffer if the activity of water (a_{H_2O}) in the sample is 1. Otherwise, the deviation is given by

$$\Delta \log fO_2 = 2 \log(a_{H_2O}^{sample}) \text{ (e.g., Sisson et al. 2005; Matjuschkin et al. 2015).}$$

In this study, all run products are fluid-saturated, but due to the presence of CO_2 in the starting mix, the $a_{H_2O}^{sample} < 1$ and must be estimated from

$$a_{H_2O} = \frac{f_{H_2O}^{fl} \cdot \gamma_{H_2O}^{fl}}{f_{H_2O}^0}$$

where $f_{H_2O}^{fl}$, $\gamma_{H_2O}^{fl}$ are fugacity and activity coefficient of H_2O in mixed fluid and $f_{H_2O}^0$ is the fugacity of pure H_2O at pressure and temperature of interest. $f_{H_2O}^{fl}$ can be calculated for each run via

$$f_{H_2O}^{fl} = P \cdot X_{H_2O}^{fl} \cdot \Gamma_{H_2O},$$

where P is pressure; $X_{H_2O}^{fl}$ is the mol fraction of water in fluid; and Γ_{H_2O} is the fugacity coefficient of H_2O at pressure, temperature conditions. The latter was calculated using the equation of state (EOS) of Churakov and Gottschalk (2003) for

each experimental pressure and temperature. Depending on the oxygen buffer used, X_{H_2O} and a_{H_2O} in fluid were either calculated by mass balance, estimated from H₂O-CO₂ solubility relationships, or determined from phase diagrams provided by Woermann and Rosenhauer (1985). The following volatile components were calculated to be stable at the various experimental run conditions: H₂, H₂O, CO₂, CO, CH₄, SO₂ and H₂S. Concentrations of other element oxides (e.g. SiO₂, Al₂O₃) in fluids are not well known for our system at these conditions (Newton and Manning 2008; Sverjensky et al. 2014), but are thought to be relatively low, given that a_{SiO_2} and $a_{Al_2O_3}$ in runs are less than one (quartz and corundum are not present). Nevertheless, error bars on fO_2 values were extrapolated in a conservative manner and give some idea of the effect of minor fluid components (incl. S, Cl).

2.3.1 Runs buffered at Re-ReO₂ and H-M.

The Churakov and Gottschalk (2003) model suggests that CO₂ and H₂O are the dominant constituents of fluids at $fO_2 \geq NNO+2$. Hence, the masses (m) of H₂O and CO₂ in fluid (fl) can be estimated by mass balance calculations knowing: the amount of H₂O and CO₂ added to the starting mix (st); the concentrations of H₂O and CO₂ in quenched glasses (gl); the amount of H₂O in hydrous phases (hydr); and the fractions (X) of melt and hydrous phases:

$$mH_2O^{fl} = mH_2O^{st} - mH_2O^{gl} \cdot X^{gl} - \sum mH_2O^{hydr} \cdot X^{hydr} \quad (1)$$

$$mCO_2^{fl} = mCO_2^{st} - mCO_2^{gl} \cdot X^{gl} \quad (2)$$

$$X_{H_2O}^{fl} / X_{CO_2}^{fl} = (mH_2O^{fl} / mCO_2^{fl}) \cdot 2.44 \quad (3)$$

The fractions of minerals, melt and fluid for each run were calculated using MINSQ (Hermann and Berry 2002).

2.3.2 Runs buffered by Ni-NiO and Co-CoO.

Equilibrium reactions at $fO_2 \leq NNO$ suggest the composition of COH-fluid shifts towards increasing f_{H_2O} , f_{CH_4} , f_{CO} , a_C with decreasing f_{CO_2} owing to increasing f_{H_2} in the sample:



where $K_4 = (f_{CO_2} \cdot f_{H_2}^2) / (a_C \cdot f_{H_2O}^2)$



where $K_5 = (f_{\text{CH}_4}) / (a_{\text{C}} \cdot f_{\text{H}_2}^2)$



where $K_6 = (f_{\text{CO}}^2) / (a_{\text{C}} \cdot f_{\text{CO}_2})$

K_4 , K_5 and K_6 are equilibrium constants of reactions 4, 5 and 6 respectively.

According to EOS calculations for fluid compositions stable at f_{H_2} corresponding to NNO buffer conditions, the total mol fractions of CH_4 and CO in the fluid do not exceed 0.05%. These results are corroborated by high-pressure studies of Luth (1989) and Armstrong et al. (2015), who demonstrated that CH_4 only becomes significant at f_{O_2} below NNO-3. Although CO_2 and H_2O are still the dominant constituents of these COH-fluids, their mol fractions cannot be calculated by mass balance as a result of CO_2 breaking down to graphite and H_2O via reaction 4. Hence, molar fractions of CO_2 and H_2O in the fluid were obtained from $X_{\text{H}_2\text{O}}^{\text{fl}}$ isobars estimated from CO_2 - H_2O solubility curves calculated at $f_{\text{O}_2} \geq \text{NNO}+2$ (see Results).

The most reduced experiments performed at Co-CoO buffer conditions differ from other runs in their proximity to the graphite-C-H-O equilibrium field (Ulmer and Luth 1991) leading to extensive crystallization of graphite. In those runs the activity of H_2O was determined from graphite-fluid equilibrium diagrams of Woermann and Rosenhauer (1985). However, the amount of CH_4 and CO in these fluids is more difficult to calculate.

2.4 Analytical Methods

2.4.1 Electron microprobe (EPMA)

Compositions of experimental run products were determined using a Cameca SX-100 electron microprobe. Glasses were analysed with 10 μm defocused 4 nA beam, operating at 15 kV accelerating voltage. Minerals were analysed with 1 μm beam operating at 15 kV and 10 nA. All elements were measured on their K_{α} emission lines with 10 seconds integration time for Na, Si, K, Al; 20 seconds for Mg and Ca, 20 or 30 seconds for Ti, Fe, Cl, S. The integration time for low and high backgrounds was set at half the time of the peak value. Albite, Mg-rich olivine, sanidine, wollastonite, BaSO_4 (sulphate), FeS_2 (sulphide), ilmenite and NaCl were used as standards. The calculated detection limit for S in glasses at the analytical conditions is about 90 ppm. Some of

the lower S measurements in reduced condition experiments were cross-checked at 20 kV and 50 nA. For one particular NNO run at 1.0GPa, 900°C the S value was confirmed to be around the detection limit of 90 ppm.

2.4.2 Secondary ion mass spectrometry (SIMS)

Secondary ion mass spectrometry (SIMS) analysis of H₂O and CO₂ (as ¹H and ¹²C) in the glasses was carried out using the NERC Cameca IMS 4-f ion microprobe at the University of Edinburgh with a primary beam of negative ¹⁶O⁻ ions, a beam current of 5 nA and a total impact energy of 14.5 keV. CO₂ was measured with a mass resolution of 1200 to differentiate between ²⁴Mg²⁺ and ¹²C⁺. Filtering of the secondary beam led to detection of only ions with 50±20 eV. H₂O analyses on the same spots were performed separately at lower mass resolution (500) with an energy window of 75 ±20 eV. Working curves were established using calibrations on basaltic, andesitic and rhyolitic glass standards with volatile contents up to 10.5 wt % H₂O and 1.1 wt % CO₂.

3. Results

Experimental conditions, composition of fluids, and phase proportions are presented in Table 2. Compositions of mineral phases and quenched glasses are listed in Table 3. The euhedral habit of solid phases, lack of observable zoning, and presence of metal+oxide in the buffer all suggest the runs reached equilibrium in the 3-4 day run duration (the required equilibrium time is discussed at length in Matjuschkin et al. 2015). Although no reversals were attempted, the clear shift of the sample from the loaded fO₂ and S²⁻/S⁶⁺ ratio to both higher and lower values also gives confidence that equilibrium was achieved.

3.1 Run Products

3.1.1 Textures.

Representative images of run products are presented in figure 2a-c. All runs have crystals and glass (quenched silicate melt), and are fluid-saturated. The presence of excess fluid is indicated by vesicles (bubbles), whose distribution in the capsule is not homogeneous and shows a clear tendency to nucleate near crystals or capsule

walls, sometimes forming voids. In the oxidized (HM) runs the vesicles are bigger (up to 50 μm), whilst in the graphite-bearing runs they are rarely $> 5 \mu\text{m}$. With increasing temperature melt fraction increases and fluid fraction decreases, as best seen in Fig. 2d. The size of mineral grains varies from 5 to $\sim 35 \mu\text{m}$ (Fig. 2a,b). Silicates and oxides exhibit euhedral/subhedral crystal forms and are homogeneous in chemical composition. Sulphides occur as anhedral, rounded or subangular 1-3 μm grains and occasionally as bigger 5-20 μm aggregates (Fig. 2a). Most of the EPMA analyses made on small sulphide grains had to be screened for contamination by neighbouring crystals or melt. Anhydrite forms $\sim 10 \mu\text{m}$ long and 0.5-1 μm wide lath-shaped crystals (Fig. 2b), that are difficult to analyse. Retaining anhydrite during sample preparation requires special attention and it can easily be lost. The anhydrite composition is not reported here but its presence was confirmed by EDS analyses and Raman spectroscopy. Amphibole and plagioclase are present, sometimes forming mineral clots (Fig. 2a,c). In reduced runs, graphite forms platy, acicular crystals that are difficult to polish and, in a similar fashion to fluids, tend to form around silicate crystals especially near the capsule wall (Fig. 2c).

3.1.2 Phases Relations.

Phase relations are plotted as a function of temperature and $f\text{O}_2$ at 1.0 GPa in figure 3a and at 1.5 GPa in figure 3b. Modal proportions of phases are shown in figure 4 and are discussed below for each $f\text{O}_2$ series.

The most oxidized experiments were buffered by HM ($\Delta\text{NNO} \approx +4.75$) and only run at 1.0 GPa. These are characterised by abundant amphibole, plagioclase and magnetite (Fig. 4). Anhydrite (CaSO_4) is present, associated with sulphur-rich melt (see Melt Composition). Melt fraction increases from 47 to 49 wt% with increasing temperature, whilst the fluid fraction was calculated to be ~ 2.5 wt% for all three runs.

A single 0.5 GPa run was performed at Re-ReO₂ buffered conditions ($\Delta\text{NNO} \approx +2$) and 900°C (not included in Fig. 3). The run product is similar to the HM series and consists of amphibole, plagioclase, magnetite, and anhydrite. However, this run has a higher melt fraction (60 wt%) and higher exsolved fluid content (~ 3 wt%). The sulphur content in the melt is the highest value observed in this study (see Melt Composition). It should be noted that the occurrence of anhydrite at this $f\text{O}_2$ and

higher (HM runs) is consistent with previous studies at similar or lower pressures (Jugo et al. 2010; Botcharnikov et al. 2010).

The higher pressure Re-ReO₂ experiments produced surprising results. Those performed at 1.0 GPa demonstrate the presence of amphibole, plagioclase and magnetite, but are saturated with pyrrhotite (FeS) instead of anhydrite, which was unexpected. With increasing temperature from 850 to 950 °C melt fraction increases from 34 to 67 wt% and fluid fraction decreases from 3.9 to 2.2 wt%. The Re-ReO₂ runs at 1.5 GPa have clinopyroxene at 950°C, garnet at 900, 950°C (and presumably at 850°C), but both plagioclase and amphibole are absent at 950°C. Magnetite is absent at all temperatures owing to the presence of garnet; instead ilmenite was found to be present, but only at 850°C. Re-ReO₂ runs at 1.5 GPa have pyrrhotite, and lack anhydrite. Melt fractions are higher compared to 1.0 GPa runs and decrease from 80 to 47 wt% with decreasing temperature. Owing to increasing solubility of water and CO₂ in the melt (e.g. Ghiorso and Gualda 2015), the calculated fluid fraction at 1.5 GPa is lower than at 1.0 GPa and varies from 1 to 2.5 wt% with decreasing temperature.

The runs buffered at NNO ($\Delta\text{NNO} \approx 0$) resemble the more oxidized runs in their mineral assemblage, although magnetite is absent and Ti-rich ilmenite occurs in all 1.0 GPa runs. At 1.0 GPa and 950°C plagioclase crystallisation is suppressed resulting in ~14 wt% higher melt fraction compared to more oxidized runs performed at the same temperature and Re-ReO₂. A feature of the NNO experiments is the appearance of titanite at 850°C and 1.5 GPa. All NNO-buffered runs have pyrrhotite (sulphide-saturated), as expected from previously published experiments (e.g. Carroll and Rutherford 1987; Jugo et al. 2010).

The most reduced experiments in this study, buffered at Co-CoO ($\Delta\text{NNO} \approx -1.7$) differ significantly from other runs in terms of mineral assemblage, crystallinity and fluid composition. At these pressures the calculated Co-CoO buffer should lie close to the graphite-C-O-H fluid equilibrium (C-CHO), although the latter is more pressure sensitive (see Melt Composition). Due to the close proximity of these two buffers, the entire suite of 1.5 GPa experiments contains aggregates of acicular graphite, but at 1.0 GPa, graphite was identified only in one run performed at 900°C (Fig. 2c), suggesting other two other runs may have experienced an imposed $f\text{O}_2$ lying at or just above the graphite-C-H-O boundary. A further distinctive feature of the Co-CoO

experiments is the absence of plagioclase at all pressure and temperature conditions, and an associated high proportion of melt, 70 to 88 wt% (Figure 4). This is consistent with the observations of Freise et al. (2009) suggesting that the stability field of plagioclase becomes more sensitive to melt water content with decreasing fO_2 . Hence, at a given pressure, temperature and melt composition, crystallisation of plagioclase can be suppressed by reducing fO_2 . Titanite is present below 900°C at both pressures. Ilmenite was identified for the entire suite of 1.0 GPa runs and in a single run at 850°C at 1.5 GPa. Owing to the formation of graphite at the expense of CO_2 , the amount of fluid at NNO-1.7 is significantly less than the more oxidized runs; estimated to be <1 wt% (Fig. 2e).

3.1.3 Solid Phase Compositions

Amphibole and Plagioclase. Even though the experiments span a wide range of temperatures and fO_2 , the composition of amphibole appears to be sensitive only to pressure. Thus, Al contents increase from 1.76 cations per formula units (c.p.f.u.) at 0.5 GPa to 2.25 at 1.0 GPa and 3.05 at 1.5 GPa. With increasing pressure K and Na contents increase and Mg decreases. In comparison to 1.5 GPa runs, experiments performed at 1.0 GPa demonstrate lower Ti and higher Ca values.

Anorthite content of plagioclase varies from 26 to 42 mol% and increases with increasing temperature. Temperatures calculated using the plagioclase-hornblende thermometer (Holland and Blundy 1994) are in excellent agreement with experimental temperatures and deviate by $\leq 7^\circ C$ with exception of one Re- ReO_2 experiment at 1.5 GPa, 850 °C where temperature is underestimated by 26°C. Given the apparent high accuracy and precision, this thermometer was favoured to the thermocouple temperature in HM-buffered runs where, as noted above, the high fO_2 conditions caused partial oxidation of the thermocouple wire.

Clinopyroxene is limited to runs at 1.5 GPa and 950 °C. They are Al-Na-rich augites with Mg# from 0.64 to 0.75 with a minimal range in Na, Ca, Mg, Ti and Fe. Total Al contents range from 0.29 to 0.42 c.p.f.u. and increase with increasing fO_2 .

Garnet is only observed at 1.5 GPa, where it is present in almost all runs apart from the melt-rich, higher temperature runs at the lowest fO_2 (see Fig. 3). In NNO runs,

garnet is a significant phase at 950°C with 14 wt%. In contrast, at 850°C it is only present as a minor component (<5 wt%). All garnets have high Fe contents (1.27 to 1.54 c.p.f.u.) increasing with decreasing temperature along with Ca, whose content ranges from 0.6 to 1.12 c.p.f.u.. Mg contents vary from 0.52 to 1.24 c.p.f.u. and increase with increasing temperature.

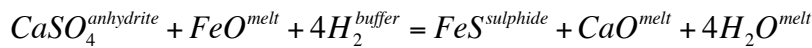
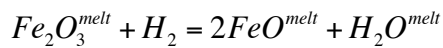
Oxides. At 1.0 GPa ilmenite is stable at reduced conditions ($fO_2 \leq NNO$) and is characterized by high TiO_2/FeO ratios, whilst magnetite is stable at $fO_2 \geq NNO+2$ with a much higher FeO content. At $fO_2 < NNO+2$ magnetite and ilmenite are minor phases and comprise less than 1 wt% of run products. Only at $NNO+4.7$ is the magnetite fraction higher, ranging from 2.1 to 3.6 wt%. Hematite is not observed in these run products as $a_{H_2O} < 1$ leads to a fO_2 value slightly below the HM buffer. At 1.5 GPa ilmenite is present at all fO_2 conditions at 850°C, but not at higher temperatures, whereas magnetite is absent due to the presence of garnet. Similar to 1.0 GPa runs, the Fe-content in ilmenite increases with increasing fO_2 .

3.1.4 Melt Composition

Major Elements. On a total alkali-silica (TAS) diagram (Le Bas et al. 1986) the volatile-free composition of the starting material is trachyandesite (57.2 wt% SiO_2), whilst the compositions of quenched silicate glasses are trachydacitic, with SiO_2 concentrations increasing from 60 to 69 wt% with decreasing temperature (Fig. 5). The total concentration of Na_2O+K_2O ranges from 7.4 to 9.3 wt% and increases with decreasing temperature with the exception of one Co-CoO-buffered experiment at 1.0 GPa and 850 °C, where the total alkali concentration decreases by 0.5 wt% relative to the 900 °C run. Overall, irrespective of fO_2 , the concentrations of TiO_2 , Al_2O_3 , FeO, MgO, CaO decrease with decreasing temperature owing to crystallization of silicate phases (amphibole, plagioclase, garnet, clinopyroxene) and oxides (magnetite, ilmenite). As plagioclase stability is sensitive to fO_2 (Figs. 3 and 4), the concentrations of Al_2O_3 and CaO in the melt demonstrate a clear tendency to follow distinct redox trends. At any given temperature, the most reduced runs exhibit the highest Al_2O_3 and CaO concentrations, whereas in the more oxidized runs these are lower by 1.3-2.3 and 0.5-1.7 wt% respectively. For runs at intermediate fO_2 (NNO) Al_2O_3 and CaO concentrations lie between these extremes (Fig.6).

Dissolved Volatiles.

The H₂O and CO₂ contents in silicate glasses as analysed by ion probe are shown in figure 7a for 1.0 and 1.5 GPa runs. The water content of the melt increases with decreasing temperature owing to progressive crystallization of dominantly anhydrous minerals, even when amphibole is stable. CO₂ decreases as fluid X_{H_2O} increases (see below). In general, oxidized melts exhibit somewhat lower H₂O concentrations compared to more reduced experiments. This is related to formation of CaSO₄ and/or increase in ferric iron, both sequestering oxygen from the melt, and liberating hydrogen. In reduced experiments increasing FeO content and the stabilization of sulphides and graphite lead to higher H₂O values, consistent with the observed destabilisation of plagioclase at lower fO_2 . As bulk water content is a function of fO_2 and phase composition its deviation from run to run can be estimated by the following mass balance:



Ferric-ferrous ratios in melt can be estimated using Kress and Carmichael (1991). Thus, the bulk H₂O content in the NNO+4.8 suite of experiments is 0.5 wt% lower compared to NNO+2 and 1.45 wt% higher at NNO-1.7, assuming that for these graphite-saturated runs a substantial part of CO₂ is reduced to C+H₂O via equation 4. The covariation of H₂O with CO₂ is illustrated in figure 7b and the oxidized experiments at 0.5 and 1.0 GPa fall approximately on isobars calculated from the solubility model of Ghiorso and Gualda (2015). The 0.5 GPa runs yield calculated pressures of 0.43 GPa, suggesting that the true pressure of these runs is lower than their nominal 0.5 GPa value (Pistone et al. 2016). Some of the more reduced 1.0 GPa experiments at Co-CoO fall well below the H₂O-CO₂ isobar. Some of the 1.5 GPa data fall in the region expected for higher pressure, but again the reduced runs at Co-CoO (all graphite-saturated) fall well below the expected CO₂ and H₂O values. This suggests an insoluble species (CO or CH₄) dilutes these components in the fluid.

The concentration of Cl in melts increases slightly with decreasing temperature in response to the increasing crystal fraction (Fig. 6). However, when the relative mass of residual melt is taken into account, a significant amount of Cl appears to be lost to

the fluid. It should be noted that we did not include P_2O_5 in the starting composition, so apatite cannot form to sequester the Cl, although some Cl is incorporated in amphibole in concentrations from below detection up to 1400 ppm with decreasing temperature (table 3).

Sulphur contents of the melts (Figure 6) are controlled dominantly by the fO_2 and buffering by solid S-bearing phases and temperature (at high fO_2) rather than the proportion/composition of melt or fluid. The 1.0 GPa experiments at HM ($\Delta NNO \approx +4.75$) have anhydrite as the stable S-bearing phase. This is associated with high dissolved sulphur contents in melt; 390, 680 and 600 ppm at 841, 870 and 875°C respectively.

The single anhydrite-bearing Re-ReO₂-buffered run at 900°C and 0.5 GPa has a melt sulphur content of ~1030 ppm, which is the highest value of all runs in this study. The Re-ReO₂ experiments performed at 1.0 GPa, and saturated with pyrrhotite (FeS) instead of the expected anhydrite, have a sulphur content strongly increasing with temperature from 480 ppm at 850°C to 970 ppm at 950°C, suggesting some influence of a sulphate species in the melt. At 1.5 GPa the Re-ReO₂. pyrrhotite-bearing runs had melts with lower sulphur contents restricted to a range from 460 to 340 ppm suggesting less influence of any sulphate species.

NNO-buffered experiments have the lowest S concentrations with an average of 150 ± 74 and 165 ± 43 ppm at 1.0 and 1.5 GPa respectively. This is approaching the detection limit using EMPA and it is difficult to identify any pressure- or temperature-related trends. Experimental glasses at the Co-CoO buffer have slightly higher sulphur contents of 217 ± 56 and 315 ± 75 ppm at 1.0 and 1.5 GPa, respectively, with a tendency to increase with increasing temperature.

3.1.5 Fluid composition

Measuring the H₂O and CO₂ contents of the melt allows an estimate of the experimental fluid compositions by mass balance (see Methods). Excess C-O-H fluid was indicated by the presence of vesicles and voids in run products, with size, form and quantity varying with pressure, temperature and oxygen fugacity. The estimated molar X_{H_2O} ranges from 0.70 to 0.85 and increases with decreasing temperature due to crystallisation of anhydrous phases (Fig. 7a). Calculated activity of water (a_{H_2O})

varies between 0.75 and 0.87 (see table 2); hence, the fO_2 is reduced by -0.25 to -0.12 log units relative to the buffer.

In contrast to the oxidized runs, experiments at NNO and Co-CoO approach or lie within the graphite stability field respectively. Graphite formation is driven by continuous breakdown of CO_2 owing to increasing fH_2 (decreasing fO_2) (see Luth 1989). Graphite was not identified in any NNO runs or in NNO-1.7 runs at 1.0 GPa and 850, 950°C. However, it is present in the entire set of NNO-1.7 experiments at 1.5 GPa and in a single run at 900°C, 1.0 GPa. In those, the fO_2 must lie below the graphite-C-O-H fluid equilibrium (Ulmer and Luth 1991). As carbon partitions into graphite, less is available for fluid species and X_{H_2O} increases. Water content of reduced fluids at NNO was reconstructed from $X_{H_2O} - X_{CO_2}$ solubility isopleths, previously determined at Re-ReO₂ and HM buffered conditions (ignoring any minor CO or CH₄). Fluid compositions of NNO runs are similar to those reported for $\Delta NNO+2$.

At fO_2 conditions corresponding to the Co-CoO buffer a different approach has been used to determine the composition of fluid. The run at 1.0 GPa and 950°C lacks graphite, which is perhaps not surprising as the calculated Co-CoO buffer only lies 0.1 ± 0.35 log units below the graphite-COH fluid equilibrium. The lack of graphite means the ratio of water and CO_2 that dominate the fluid can be estimated using the method described for NNO runs giving $X_{H_2O} = 0.78$ and a solubility that falls on the 1.0 GPa isobar in figure 7b. In contrast, at 900 and 850°C Co-CoO buffered runs should lie further into the graphite stability field at 0.3 ± 0.35 and 0.4 ± 0.35 log units below graphite-C-O-H fluid equilibrium. At 900°C graphite is indeed observed, whilst at 850°C it was not identified, although the measured amount of CO_2 in the melt is less than at 950°C (see Fig.7a). Hence, the 1.0 GPa 900°C run lies in the graphite stability field, whilst the 850°C run might lie slightly above it. The estimated a_{H_2O} at 850 and 900°C is 0.72 (+0.18/-0.25) and was calculated from

$$a_{H_2O} = 10^{(0.5\Delta \log fO_2)} \text{ (Matjuschkin et al. 2015),}$$

where the $\Delta \log fO_2$ is the deviation of Co-CoO buffer from graphite-C-O-H fluid equilibrium. Overall, the measured C content in these lower temperature Co-CoO buffered melts is much lower in comparison to 950°C (Fig.7a) and well below the 1.0 GPa isobar in Figure 7b. This suggests that the excess fluid contains a significant

amount of an insoluble species, either CO or CH₄, reducing the CO₂ fugacity (Pawley et al. 1992; Thibault and Holloway 1994; Morizet et al. 2010).

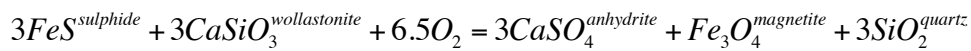
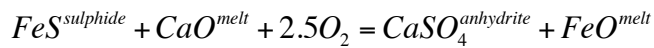
The 1.5 GPa suite of experiments is 0.7 to 1 log units more reduced than the graphite-COH buffer, contains graphite, and has an estimated water activity of $\sim 0.7 \pm 0.2$. Again the measured C in melt (expressed as CO₂) is even lower than the value estimated from the oxidized 1.5 GPa experiments in Fig. 7b, falling well below even the 1.0 GPa isopleths. This cannot be explained by an even higher activity of water and again appears to reflect high activities of insoluble CO or CH₄ in the fluid.

Unfortunately, it was not possible to estimate the amount of sulphur entering the fluid using the mass balance calculations due to the large amount of S incorporated in solid S-bearing phases. Thus, errors in estimating the small amounts of sulphide or sulphate have significant effect on the mass balance. However, we were able to make an estimate of sulphur partition coefficient between fluid and melt for a single super-liquidus run (Table 1) at 1.0 GPa, ~ 1120 °C and NNO+4.7 and with a resulting high S content. This suggests a calculated $D^{\text{fl/melt}} \sim 0.1$. Using this value for oxidized conditions $\Delta\text{NNO} \geq \pm 2$ the mol fraction of S in the fluid (X_S) is negligible. For reduced, Co-CoO buffered conditions the fluid/melt partition coefficient of sulphur has been reported as 468 at 0.2 GPa and 850 °C (Keppler 2010) and using this value our reduced fluid S may be as much as $X_S < 0.026$ mol%. Other partition coefficients are reported in the literature (e.g. Scaillet et al. 1998), but using any of these still suggests the amount of S-species in the fluid remains insignificant in the context of this study. The systematics of S-partitioning in fluid as a function of fO_2 at high-pressure conditions requires further experimental investigation.

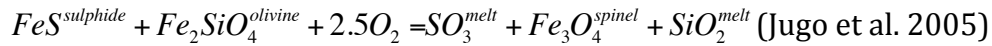
4. Discussion

Sulphur content and speciation in silicate melts are often used as monitors of magmatic fO_2 conditions (e.g. Kress 1997), but this is only really possible when the bulk S concentration are in the lower ppm range. As concentrations reach weight per cent levels, sulphur can itself act as a strong oxygen buffer rather than a sensor owing to its high redox capacity, i.e. eight electron transfer from S²⁻ to S⁶⁺. It is for this reason that subducted sulphate has been suggested as a potential oxidant of the mantle wedge in sub-arc environments (Evans and Tomkins 2011). Buffering with

sulphur at magmatic conditions operates via various heterogeneous equilibria such as:



(Carroll and Rutherford 1987)



In this study, fO_2 is set by an external buffer and sulphur speciation is forced to conform to the imposed fO_2 conditions, although its concentration is in the range expected for natural magmas (Wallace 2005). Redox conditions clearly affect the solubility of sulphur (sulphate and sulphide species) in the melt, but it should be noted that solubility is also a function of melt composition, sulphur fugacity, activity of water and CO_2 in the melt and pressure, temperature conditions (Mavrogenes and O'Neill 1999; Liu et al. 2007; Beermann et al. 2011; Masotta and Keppler 2015). As a result, our experiments are not directly applicable to all natural magma systems, but are relevant to subduction zone magmas and, more importantly, illustrate some key principles, as outlined below. As all run products are saturated either in pyrrhotite or anhydrite; the measured sulphur content also establishes the Sulphur Concentration at Sulphide Saturation (SCSS) or Anhydrite Saturation (SCAS) for a trachydacite melt generated from a basaltic trachyandesite parent by mid to lower crustal differentiation.

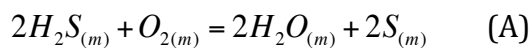
4.1 Effect of pressure and fO_2 on sulphur speciation and solubility

Published experimental data on sulphur speciation in silicate melts at 0.2 GPa suggest the sulphate-only stability field is reached at $\Delta NNO \geq 1.5$ and the transition from sulphide to sulphate takes place over a narrow fO_2 window of 2 log units (Jugo et al. 2010; Botcharnikov et al. 2010; Masotta and Keppler 2015). Whilst our 0.5 GPa experiment at $NNO+2$ (Re- ReO_2 buffer) contains anhydrite consistent with these previous studies, our higher pressure results show pyrrhotite persists above $NNO+2$. Evidently the sulphide stability field expands towards higher fO_2 with increasing pressure.

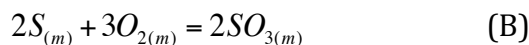
In order to reconstruct the new sulphide-sulphate stability fields at 1.0 and 1.5 GPa, knowledge of sulphate content and fO_2 of the melt for each run is required. Whereas

the latter parameter is well constrained, our experimental samples are not amenable to determination of sulphur speciation using EPMA (Carroll and Rutherford 1988), as low sulphur content in the melt leads to high measurement uncertainties (Matthews et al. 1999) not to mention other problems such as S-peak migration and sulphide oxidation with a static beam. It also proved impossible to fit our data to the SCSS algorithm of Mavrogenes and O'Neill (1999) and Liu et al. (2007) to calculate dissolved sulphate content by difference. The problem of this approach is the unexplained minimum in SCSS at $fO_2 \approx NNO \pm 0.5$, which was found in all the experimental series in this study and is apparent from the datasets of other workers in Fe-bearing systems (e.g. Katsura and Nagashima 1974; Carroll and Rutherford 1985, 1987; Jugo et al. 2005; Clemente et al. 2004; Botcharnikov et al. 2010) and Fe-free (e.g. Nagashima and Katsura, 1973). This phenomenon is often ascribed to the changing Fe^{2+} content in melt, yet in our experiments (and others) it has little correlation with silicate melt composition, Fe^{2+}/Fe^{3+} , fH_2S or fS_2 (Carroll and Rutherford 1985; Clemente et al. 2004; Nagashima and Katsura 1973).

One possible explanation for the minimum in the SCSS value is the formation of an 'intermediate' oxidation state sulphur-species existing in the fO_2 range between sulphide (S^{2-}) and sulphate (S^{6+}). If this species has low solubility in the silicate melt and lacks an equivalent magmatic solid phase then it will partition strongly into the fluid producing a minimum in the solubility curve. Moreover, if this species is present at low concentrations (low solubility) or is kinetically difficult to retain during quenching, it may be undetectable by common spectroscopic methods. For algebraic simplicity in the following we consider this intermediate species to be S^0 (i.e. elemental sulphur), but we stress that any relatively insoluble species with an intermediate oxidation state between S^{2-} to S^{6+} oxidation will suffice (S^{4+} , S^- or S_3^- , see below and the example in Fig. S3). For the case of S^0 , equilibrium can be described by the following reactions and equilibrium constants (K):



$$K_{A(P,T)} = \frac{f_S^2 \cdot f_{H_2O}^2}{f_{O_2} \cdot f_{H_2S}^2} \cong \frac{X_S^2 \cdot a_{H_2O}^2}{f_{O_2} \cdot X_{S^{2-}}^2}$$



$$K_{B(P,T)} = \frac{f_{SO_3}^2}{f_{O_2}^3 \cdot f_{S^0}^2} \cong \frac{X_{S^{6+}}^2}{f_{O_2}^3 \cdot X_{S^0}^2}$$

where $S^0_{(m)}$ is the proposed intermediate oxidation state S-species.

If the proportions of all sulphur species, S^{6+} , S^{2-} or S^0 , are now defined, the ratios R_6 , R_2 and R_0 give their amount in respect to the total sulphur content in the melt and are defined as follows:

$$R_6 = \frac{X_{S^{6+}}}{X_{S^{6+}} + X_{S^{2-}} + X_{S^0}}$$

$$R_2 = \frac{X_{S^{2-}}}{X_{S^{6+}} + X_{S^{2-}} + X_{S^0}}$$

$$R_0 = \frac{X_{S^0}}{X_{S^{6+}} + X_{S^{2-}} + X_{S^0}}$$

Substitution of sulphide and sulphate parameters from equations A and B

$$X_{S^{6+}} = K_B^{1/2} f_{O_2}^{3/2} X_{S^0} \quad \text{and}$$

$$X_{S^{2-}} = K_A^{-1/2} f_{O_2}^{-1/2} X_{S^0} a_{H_2O} \quad \text{yield:}$$

$$R_6 = \frac{1}{1 + a_{H_2O} (K_A K_B)^{-1/2} f_{O_2}^{-2} + K_B^{-1/2} f_{O_2}^{-3/2}}$$

$$R_2 = \frac{a_{H_2O} K_A^{-1/2} f_{O_2}^{-1/2}}{1 + a_{H_2O} K_A^{-1/2} f_{O_2}^{-1/2} + K_B^{1/2} f_{O_2}^{3/2}}$$

$$R_0 = \frac{1}{1 + K_B^{1/2} f_{O_2}^{3/2} + a_{H_2O} K_A^{-1/2} f_{O_2}^{-1/2}}$$

Since a_{H_2O} and f_{O_2} are known for each run, the ratios of S^{6+} , S^{2-} or S^0 are functions of K_A and K_B , which can be estimated from the experimentally obtained S-solubility data. Calculation of K_A and K_B using thermodynamic data by Robie et al. (1978) and Holland and Powell (1998) yields constant $\log K_B / \log K_A = 1.78$, with values of both K_A and K_B increasing with the decreasing temperature.

The resulting sulphur speciation model is displayed in figure 8a and illustrates the stability fields of sulphide, sulphate and intermediate sulphur species at different pressure-temperature conditions. The model was obtained by fitting both K_A and K_B to measurements of S-contents in melt (Fig. 8b; for calculated $K_{A,B}$ values and uncertainty see supplementary materials Fig.S2). Note that calculations can be equally performed using other sulphur species with intermediate oxidation state, such as S_3^- or S^{4+} . The algebraic treatment is similar and the calculated speciation curves have broadly similar shape, although S^{4+} persists to a high fO_2 . Our preliminary tests with a variety of S-species suggest that S^0 gives the closest fit to our experimentally obtained data (for comparison S^{4+} -fit see Fig.S3). However, other intermediate sulphur species, or indeed multiple other species, could be invoked. Our sulphur speciation model (Fig.8c) illustrates the strong effect of pressure on the stability fields of sulphide and sulphate. With increasing pressure the stability field of sulphide expands towards oxidized conditions. Thus, the sulphate-only stability fields at 1.0 and 1.5 GPa now lie at NNO+3 and NNO+3.5, respectively, 1 and 1.5 $\log fO_2$ units higher than at 0.2 GPa (Jugo et al. 2010, Botcharnikov et al. 2010).

4.2 Evidence for an intermediate sulphur species

Although the model presented to explain the minimum in dissolved sulphur content at $NNO \pm 0.5$ is based, for simplicity, on the presence of S^0 as the intermediate oxidation state species, it is useful to explore other possible species. The most obvious candidate currently proposed in the literature is sulphite (S^{4+}), which is the equivalent of SO_2 in the fluid, but has no obvious magmatic solid expression, i.e. there are no known magmatic sulphite minerals. This species is predicted by molecular simulation (Machacek et al. 2010) and S^{4+} has been identified in quenched silicate melts using XANES. Much of the initially identified S^{4+} in melt inclusions has now been ascribed to beam-induced reduction of S^{6+} (Backnaes et al. 2008; Wilke et al. 2008; Métrich et al. 2009). However S^{4+} has been unambiguously identified, together with S^{6+} , in some Fe-free experimental glasses in equilibrium with $CaSO_4$ at 0.4 to 1.6 GPa (Métrich et al. 2009). Although not strictly performed under controlled fO_2 , their results suggest that there may be an fO_2 window near NNO where S^{4+} has a low, but finite, solubility in silicate melts at high pressure, perhaps dissolved as molecular SO_2 . S^{4+} might be absent at higher fO_2 (or in high-Fe samples) because only S^{6+} is

stable. Alternatively it may remain unidentified due to an electron exchange reaction with Fe^{3+} ($\text{S}^{4+} + 2\text{Fe}^{3+} = \text{S}^{6+} + 2\text{Fe}^{2+}$) that proceeds readily upon quenching (Berry et al. 2006).

An alternative intermediate oxidation state sulphur species is the trisulphur S_3^- ion, which is known to be stable in aqueous solutions at temperatures $\geq 250^\circ\text{C}$ and pressures above 0.01 GPa breaking down to S^{6+} , S^{2-} and native S^0 at lower pressure-temperature conditions (Pokrovski and Dubrovinsky 2011; Pokrovski et al. 2015). It remains unclear if the trisulphur ion can exist at magmatic conditions and, if so, what its solubility in silicate melts might be. Experimental observations clearly indicate S_3^- coexistence with pyrrhotite, and S_3^- has been shown to form an ionic complex with Au in aqueous fluids (Pokrovski et al. 2015). Interestingly a recent experimental study by Botcharnikov et al. (2010) reported a sharp increase in gold solubility in silicate melt over a narrow range of $f\text{O}_2$ corresponding to the sulphide-sulphate transition at 0.2 GPa, which may indicate the stability of AuS_3 complexes in the melt at ppb levels. Preliminary measurements for Au on the samples of this study also suggest a similar maximum coinciding with our S solubility minimum. The tendency for trisulphur to break down to other S-species at low temperature conditions might be responsible for the formation of anhydrite-bearing, water-rich melts, which are often found as melt inclusions in epithermal gold deposits (e.g. Chamberfort et al. 2008). Such deposits might represent a quench product of AuS_3 complexes. The partitioning of trisulphur between fluid and silicate melt is unknown, so our proposed effect on S solubility in the melt is speculative. It also remains unclear how this species might affect the composition of sulphides, which are often used to estimate sulphur fugacity at magmatic P-T conditions (e.g. Froese and Gunter 1976; Clemente et al. 2004).

Note that it is a simple matter to recast equations (A) and (B) above in terms of S_3^- (or S^{4+}) rather than S^0 ; the essential form of Figure 8 will remain unchanged. If the modelled intermediate species in Fig. 8 is trisulphur this suggests a narrow $f\text{O}_2$ -window of stability.

4.3 Implication for the formation of porphyry copper deposits

Experimental evidence for the shift of the sulphide stability field towards oxidized conditions with increasing pressure has consequences for the behaviour of

chalcophile elements in magmatic reservoirs at mid- to deep-crustal depths (≥ 15 km). In particular, Cu is likely to be depleted even in the more oxidized magmas found in arc systems, due to strong partitioning into any dense immobile sulphide phase (sulphide melt or solid pyrrhotite) that remains trapped in deep cumulates. The prevention of deep sulphide saturation via oxidation alone would require either very high fO_2 conditions $\Delta NNO \geq 3$. This may be unrealistic even for sub arc magmas (Fig. 1a, and 9), although the extreme requirements of this condition could be linked to the rarity of PCDs.

An alternative means to suppress sulphide formation in the roots of volcanic arcs is if the parental magmas remain S-poor (< 100 ppm S). This requires that the primary magmas themselves are S-poor, again an unusual situation for arc basalts (Wallace 2005) again perhaps explaining for the rarity of PCDs. Even if the magmas start with low S, the concentrations are likely to increase through extensive crystallisation to eventually approach the critical SCSS level. A more plausible mechanism for maintaining low S contents is via degassing during early stages of magmatic differentiation, as would be expected for arc magmas that are initially very rich in other volatile species, such as H_2O and, particularly, CO_2 . These species will exsolve to produce a fluid phase into which sulphur can partition (Muntean et al. 2011). The earlier a magmatic volatile phase separates during differentiation, the greater the ensuing depletion in S. Although, our understanding of sulphur degassing is limited to experiments at lower pressures (< 0.5 GPa), it is known to be a strong function of melt composition and oxygen fugacity, with $D_s^{fluid/melt}$ increasing with increasing degree of silicate melt polymerization and decreasing fO_2 respectively (Keppler 2010; Webster and Botcharnikov 2011; Zajacz 2015). Regardless of the exact value of D_s the amount of S quantitatively stripped from the melt during degassing will be a function of the total exsolved gas budget. Thus, unusually volatile-rich, evolving magmas that begin degassing at high pressures (perhaps at CO_2 saturation) can maintain dissolved S contents that are sufficiently low to preclude sulphide saturation. The recent suggestion that arc magmas may have higher initial CO_2 contents than would be suggested on the basis of melt inclusions alone (Blundy et al. 2010) would favour early volatile exsolution. As is evident from our experimental results, preventing sulphide saturation is easier at elevated fO_2 ($> NNO$), but the increased stability of sulphide species to high fO_2 at high pressure means that it is the

abundance of other volatiles, rather than fO_2 , that could play the key role in keeping S below sulphide saturation.

We suggest that it is the combination of very high initial volatile contents coupled with the oxidized nature of arc basalts that provides the most favourable conditions for the formation of porphyry copper deposits through suppression of any early sulphide saturation that would otherwise remove Cu. In some locations the sub-arc environment favours both these conditions with subduction of sulphur- carbon- and water-rich sediments releasing S and CO_2 - H_2O fluids that dissolve in and later exsolve from the ascending magmas buffering their fO_2 above the graphite-C-H-O reaction (Ulmer and Luth 1991; Connolly 2005; Fig.9). This mechanism at least maintains the melts above a 'minimum' fO_2 at the graphite-CHO buffer (Fig. 1a, 9). In other locations the mantle might be more reduced and early (deep) exhaustion of CO_2 might result in formation of graphite or the subducted sediments are relatively CO_2 -poor. Both situations might lead to the formation of Cu-poor 'barren' magmatic systems.

Our findings also provide a potential solution to the problem of sulphide inclusions being trapped in early-formed phenocrysts in magmas that appear to have a high fO_2 , and sulphate as a stable melt phase (e.g. Mt Pinatubo, Pallister et al. 1996; Hattori 1993). If the early phenocrysts grew at high pressure, the magma could have had an initially high fO_2 (above NNO+2) and yet still crystallise sulphide (or form immiscible sulphide melt). As the magma ascends to lower pressure anhydrite becomes the stable sulphur phase without any change in the fO_2 simply because of the pressure-sensitive change in the sulphide-sulphate equilibrium. In addition any sulphide that is carried by the melt (depending on bleb size and ascent rate) will become unstable during ascent and start to dissolve in the melt, which, due to the increasing stability of S^{6+} species in the melt, can also accept more total S. Consequently, the record of early, high-pressure sulphide saturation will only be preserved as isolated inclusions in early-formed crystals.

5. Conclusions

High-pressure piston cylinder experiments reveal the effect of pressure and fO_2 on phase relations and sulphur speciation in quenched silicate melts. At the most reduced conditions imposed by the Co-CoO buffer (NNO -1.7) run products are

graphite-saturated and exhibit low amounts of fluid (<0.8 wt%), but high dissolved H₂O contents owing to breakdown of CO₂ to C which increases the water activity of the fluid. Silicate melts in these experiments exhibit high CaO and Al₂O₃ contents due to the suppression of plagioclase crystallization. This also results in an 8-30% higher melt fraction compared to more oxidized runs. Co-CoO buffered runs are characterised by the occurrence of Ti-rich phases such as titanite and ilmenite.

At NNO buffered conditions fluids are CO₂-saturated, although they lie close to the graphite stability field. Plagioclase is stable at temperatures ≤900°C and its presence yields lower Al₂O₃ and CaO contents in the melt for a given temperature relative to Co-CoO (NNO-1.7). Ti-rich ilmenite is the typical oxide phase for reduced conditions.

The series of Re-ReO₂ experiments (NNO+2) differ in many respects from those at lower fO₂ including the presence of CO₂-rich fluids, formation of Fe-rich magnetite, and absence of Ti-rich ilmenite and titanite. Plagioclase is stable in almost all runs, suggesting that its stability field increases with increasing fO₂ and becomes less sensitive to water content in the melt. As a result the Al₂O₃ and CaO contents in the melt are lower in comparison to NNO.

The most oxidized experiments buffered at hematite-magnetite (NNO+4.75) are similar to those buffered by Re-ReO₂ with the main distinguishing feature being the low Ti and very high Fe contents of magnetite.

The most surprising result is related to the stability of the sulphur-bearing phases in these experiments. At 0.5 GPa the anhydrite stability field was encountered at NNO+2 in agreement with other low-pressure studies (e.g. Masotta and Keppler 2015). In contrast, the 1.0 and 1.5 GPa NNO+2 runs contained pyrrhotite defining, for the first time, expansion of the sulphide stability field to higher fO₂ with increasing pressure. At 1.0 and 1.5 GPa, the transition to anhydrite stability is shifted ~1 and 1.5 log fO₂ units higher than at 0.5 GPa.

Implication for the formation of PCDs. Porphyry copper deposits are widely considered to be the result of copper enrichment in arc magmas during differentiation. This is most readily achieved with the suppression of any sulphide phase, which would strongly sequester Cu (partitioning values in the region of 500 for solid sulphide or 1000 for sulphide melt; Lee et al. 2012; Li and Audétat 2012; Zajacz et al. 2013). We show that suppression of sulphide is most readily achieved by deep S-degassing, which in turn requires the presence of substantial dissolved

volatiles (H_2O and CO_2) in primary magmas. In this case S partitions into the exsolved fluid phase, maintaining S contents below sulphide saturation (SCSS). Elevated $f\text{O}_2$ is also favourable to preventing sulphide saturation, but may be subordinate to the effect of high initial volatile contents (Fig.9). We agree with many previous authors that it is the volatile-rich nature of arc magmas makes them conducive to PCD formation, rather than simply their elevated $f\text{O}_2$, as claimed by others (e.g. Sun et al. 2014). Although both are typical features of arc magmas (Humphreys et al., 2015) we highlight the importance of volatile processes even in the deep arc crust.

Acknowledgments

This project was funded by a research Grant from BHP Billiton. We would like to acknowledge Charles Clapham and Donovan Hawley for maintaining the high-pressure laboratory in working condition and contributing to the development of a piston cylinder cell for the controlled $f\text{O}_2$ experiments used in this study. We also would like to thank John Mavrogenes, Brian Tattitch, Simon Kohn, Marion Louvel, Kevin Klimm, and Amy Gilmer for fruitful discussion and helpful advice. Stephan Schuth is gratefully acknowledged for providing S- and C- analyses of starting materials, Ben Buse and Stuart Kearns for help with EMPA and Richard Hinton for help with ion probe analysis.

Cited references

Armstrong LS, Hirschmann MM, Stanley BD, Falksen EG, Jacobsen ST (2015) Speciation and solubility of reduced C-O-H-N volatiles in mafic melt: implications for volcanism, atmospheric evolution, and deep volatile cycles in the terrestrial planets. *Geochim Cosmochim Acta* 171:283-302

Arai S, Ishimaru S, Okrugin VM (2003) Metasomatized harzburgite xenoliths from Avacha volcano as fragments of mantle wedge of the Kamchatka arc: Implications for the metasomatic agent. *Isl Arc* 12:233–246

Backnaes L, Stelling J, Behrens H, Goettlicher J, Mangold S, Verheijen O, Beerkens RG C, Deubner J (2008) Dissolution mechanisms of tetravalent sulphur in silicate melts: evidences from sulphur K edge XANES studies on glasses. *J Am Ceram Soc* 91: 721–727

Ballhaus C, Berry R, Green D (1991) High pressure experimental calibration of the olivine–orthopyroxene–spinel oxygen geobarometer: implications for the oxidation state of the upper mantle. *Contrib Mineral Petrol* 107(1):27–40

Ballhaus (1993) Redox states of lithospheric and asthenospheric upper mantle. *Contrib Mineral Petrol* 114:331-348

Berry A J, O'Neill HStC, Scott DR, Foran GJ, Shelley J MG (2006) The effect of composition on $\text{Cr}^{2+}/\text{Cr}^{3+}$ in silicate melts. *Am Mineral* 91:1901–1908

Beermann O, Botcharnikov RE, Holtz F, Diedrich O, Nowak M (2011) Temperature dependence of sulfide and sulfate solubility in olivine-saturated basaltic magmas. *Geochim Cosmochim Acta* 75:7612-7631

Bernard A, DeMaiffe, D, Mattielli N, Punongbayan RS (1991) Anhydrite-bearing pumice from Mount Pinatubo: Further evidence for the existence of sulphur-rich magmas. *Nature* 354:139-140

Blatter, DL, Carmichael ISE (1998) Hornblende peridotite xenoliths from central Mexico reveal the highly oxidized nature of subarc mantle. *Geology* 26:1035-1038

Blundy J, Cashman K, Rust A, Witham F (2010) A case for CO₂-rich arc magmas. *Earth Planet Sc Lett* 290:289-301

Botcharnikov RE, Linnen RL, Wilke M, Holtz F, Jugo PJ, Berndt J (2010) High gold concentrations in sulphide-bearing magma under oxidizing conditions. *Nature Geo* 4: 112-115

Brandon AD, Draper DS (1996) Constraints on the origin of the oxidation state of mantle overlying subduction zones: An example from Simcoe, Washington, USA. *Geochim Cosmochim Ac* 60:1739-1749

Brooker R, Holloway JR, Hervig RL (1998). Reduction in piston cylinder experiments: The detection of carbon infiltration into platinum capsules. *Am Mineral* 83:985-994

Camus F, Dilles JH (2001) A special issue devoted to porphyry copper deposits of Northern Chile. *Econ Geol* 96:233-237

Carmichael ISE (1991) The redox states of basic and silicic magmas: a reflection of their source regions? *Contrib Mineral Petrol* 106:129-141

Carmichael ISE, Ghiorso MS (1986) Oxidation-reduction relations in basic magma: a case for homogeneous equilibria. *Earth Planet Sc Lett* 78:200-210

Carroll MR, Rutherford MJ (1985) Sulfide and sulfate saturation in hydrous silicate melts. *J Geophys Res* 90:C601-C612

Carroll MR, Rutherford MJ (1987) Results and implication for sulphur behaviour in the 1982 El Chichon Trachyandesite and other evolved magmas. *J Petrol* 28(5):781-801

Carroll MR, Rutherford MJ (1988) Sulfur speciation in hydrous experimental glasses of varying oxidation state: Results from measured wavelength shifts of sulphur X-rays. *Am Mineral* 73:843-849

Candela PA, Holland HD (1984) The partitioning of copper and molybdenum between silicate melts and aqueous fluids. *Geochim Cosmochim Acta* 48:373-380

Chamberfort I, Dilles JH, Kent AJR (2008) Anhydrite-bearing andesite and dacite as a source for sulfur in magmatic-hydrothermal mineral deposits. *Geology* 36(9):719-722

Churakov SV, Gottschalk M (2003) Perturbation theory based equation of state for polar molecular fluids: II. Fluid mixtures. *Geochim Cosmochim Acta* 67:2415-2425

Clemente B, Scaillet, Pichavant M (2004) The solubility of sulphur in hydrous rhyolitic melts. *J Petrol* 45:2171-2196

Comodi P, Nazzareni S, Zanazzi PF, Speziale S (2008) High-pressure behaviour of gypsum: A single-crystal X-ray study. *Am Mineral* 93:1530-1537

Connolly JAD (2005) Computation of phase equilibria by linear programming: A tool for geodynamic modelling and its application to subduction zone decarbonation. *Earth Planet Sci Lett* 236:524-541

Crabtree SM, Lange RA (2012) An evaluation of the effect of degassing on the oxidation state of hydrous andesite and dacite magmas: a comparison of pre- and post-eruptive Fe²⁺ concentrations. *Contrib Mineral Petrol* 163:209-224

Dauphas N, Craddock PR, Asimow PD, Bennett VC, Nutman AP, Ohnenstetter D (2009) Iron isotopes may reveal the redox conditions of mantle melting from Archean to Present. *Earth Planet Sc Lett* 288:255-267.

Evans KA, Tomkins AG (2011) The relationship between subduction zone redox budget and arc magma fertility. *Earth Planet Sc Lett* 308:401-409

Evans KA, Elburg MA, Kamensky VS (2012) Oxidation state of subarc mantle. *Geology* 40(9):783-786

Foley SF (2011) A reappraisal of redox melting in the Earth's Mantle as a function of tectonic settings and time. *J Petrol* 52:1363-1391

Frey FA, Gerlach DC, Hickey RL, Lopez-Escobar L, Munizaga-Villavicencio F (1984) Petrogenesis of the Laguna del Maule volcanic complex, Chile (36°S) *Contrib Mineral Petrol* 88:133-149. doi 10.1016/j.epsl.2014.05.038

Freise M, Holtz F, Nowak M, Scoates JS, Strauss H (2009) Differentiation and crystallisation conditions of basalts from the Kerguelen large igneous province: an experimental study. *Contrib Mineral Petrol* 158:505-527

Froese E, Gunter AE (1976) A note on the pyrrhotite-sulphur vapour equilibrium. *Econ Geol* 71:1589-1594

Ghiorso MS, Gualda GAR (2015) An H₂O-CO₂ mixed fluid saturation model compatible with rhyolite-MELTS. *Contrib Mineral Petrol* 169:53

Gill R (2010) *Igneous rocks and processes: a practical guide*. Wiley-Blackwell, Malaysia.

Hattori K (1993) High-sulfur magma, a product of fluid discharge from underlying mafic magma: Evidence from Mount Pinatubo, Philippines. *Geology* 21:1083-1086

Herrmann W, Berry RF (2002) MINSQ – a least squares spreadsheet method for calculating mineral proportions from whole rock major element analyses. *Geochem Explor Environ Anal* 2:361-368

Holland T, Blundy J (1994) Non-ideal interactions in calcic amphiboles and their bearing on amphibole-plagioclase thermometry. *Contrib Mineral Petrol* 116:433-447

Holland TJB, Powell R (1998) An internally consistent thermodynamic data set for phases of petrological interest. *J Metamorph Geol* 16:309-343

Humphreys MCS, Blundy JD, Sparks RSJ (2006) Magma evolution and open-system processes at Shiveluch Volcano: Insights from phenocryst zoning. *J Petrol* 47:2303-2334

Humphreys MCS, Brooker RA, Fraser DG, Burgisser A, Mangan M, McCammon C (2015) Coupled interaction between volatile activity and Fe oxidation state during arc crustal processes. *J Petrol* 56:795-814

Jenner FE, O'Neill HSt C, Arculus RJ, Mavrogenes, JA (2010) The magnetite crisis in the evolution of arc-related magmas and the initial concentration of Au, Ag and Cu. *J Petrol* 51:2445-2464

Johnson KE, Davis AM, Bryndzia LT (1996) Contrasting styles of hydrous metasomatism in the upper mantle: An ion microprobe investigation. *Geochim Cosmochim Ac* 60:1367-1385

Jugo PJ, Luth RW, Richards JP (2005) An experimental study of the sulphur content in basaltic melts saturated with immiscible sulfide or sulfate liquids at 1300°C and 1.0GPa. *J Petrol* 46(4):783-798

Jugo PJ (2009) Sulphur content at sulphide saturation in oxidized magmas. *Geology* 37(5):415-418

Jugo PJ, Wilke M, Botcharnikov RE (2010) Sulfur K-edge XANES analysis of natural and synthetic basaltic glasses: implications for S speciation and S content as a function of oxygen fugacity. *Geochim Cosmochim Ac* 74:5926-5938

Katsura T, Nagashima S (1974) Solubility of sulfur in some magmas at 1 atmosphere. *Geochim Cosmochim Acta* 38:517-531

Kelley KA, Cottrell E (2009) Water and the oxidation state of subducted zone magmas. *Science* 325:605-607

Kelley KA, Cottrell E (2012) The influence of magmatic differentiation on the oxidation state of Fe in a basaltic arc magma. *Earth Planet Sc Lett* 329-330, 109-121

Keppler H (2010) The distribution of sulfur between haplogranitic melts and aqueous fluids. *Geochim Cosmochim Acta* 74:645-660

King HE, Prewitt CT (1982) High-pressure and high-temperature polymorphism of iron sulfide (FeS). *Acta Cryst B* 38:1877-1887

Kress V (1997) Magma mixing as a source for Pinatubo sulphur. *Nature* 389:591-593

Kress VC, Carmichael ISE (1991) The compressibility of silicate liquids containing Fe₂O₃ and the effect of composition, temperature, oxygen fugacity and pressure on their redox states. *Contrib Mineral Petrol* 108:82-92

Le Bas MJ, Le Maitre RW, Streckeisen A, Zanettin B (1986) A chemical classification of volcanic rocks based on the total alkali-silica diagram. *J Petrol* 27:745-750

Lee C-TA, Luffi P, Le Roux V, Dasgupta R, Albarede F, Leeman W (2010) The redox state of arc mantle using Zn/Fe systematics. *Nature* 468:681-685

Lee C-TA, Luffi P, Chin EJ, Bouchet R, Dasgupta R, Morton DM, Le Roux V, Yin Q, Jin D (2012) Copper systematics in arc magmas and implications for crust-mantle differentiation. *Science* 336:64-68

Li Y, Audétat A (2012) Partitioning of V, Mn, Co, Ni, Cu, Zn, As, Mo, Ag, Sn, Sb, W, Au, Pb and Bi between sulfide phases and hydrous basanite melt at upper mantle conditions. *Earth Planet Sc Lett* 355-356:327-340

Liu Y, Samaha N-T, Baker DR (2007) Sulfur concentration at sulfide saturation (SCSS) in magmatic silicate melts. *Geochim Cosmochim Acta* 71:1783-1799

Lowenstern JB (2001) Carbon dioxide in magmas and implications for hydrothermal systems. *Miner Deposita* 36:490-502

Luhr JF (1990) Experimental phase relations of water-saturated and sulfur-saturated arc magmas and the 1982 eruptions of El Chichon volcano. *J Petrol* 31:1071-1114

Luth R (1989) Natural versus experimental control of oxidation state: Effects on the composition and speciation of C-O-H fluids. *Am Mineral* 74:50-57

Luth RW (1989) Natural versus experimental control of oxidation state: effects on the composition and speciation of C-O-H fluids. *Am Mineral* 74:50-57

Machacek J, Gedeon O, Liska M, Marhoul F (2010) Molecular simulations of silicate melts doped with sulphur and nitrogen. *J. Non-Cryst. Solids* 356:2458-2464

Mallman G, O'Neill H (2009) The crystal/melt partitioning of V during mantle melting as a function of oxygen fugacity compared with some other elements (Al, P, Ca, Sc, Ti, Cr, Fe, Ga, Y, Zr and Nb). *J Petrol* 50:1765-1794

Masotta M, Keppler H (2015) Anhydrite solubility in differentiated arc magmas. *Geochim Cosmochim Acta* 158:79-102

Matjuschkin V, Brooker RA, Tattitch BT, Blundy J, Stamper CC (2015) Control and monitoring of oxygen fugacity in piston cylinder experiments. *Contrib Mineral Petrol* 169:9. doi 10.1007/s00410-015-1105-z

Matthews SJ, Moncrieff DHS, Carroll MR (1999) Empirical calibration of the sulphur valence oxygen barometer from natural and experimental glasses: method and applications. *Mineral Mag* 63:421-431

Mavrogenes JA, O'Neill HStC (1999) The relative effects of pressure, temperature and oxygen fugacity on the solubility of sulfide in mafic magmas. *Geochim Cosmochim Acta* 63:1173-1180

McDade P, Wood BJ, Van Westrenen W, Brooker R, Gudmundsson G, Soular H, Najorka J, Blundy J (2002) Pressure correction for a selection of piston-cylinder cell assemblies. *Mineral Mag* 66(6):1021-1028

Métrich N, Berry, AJ, O'Neill H StC, Susini J (2009) The oxidation state of sulfur in synthetic and natural glasses determined by X-ray absorption spectroscopy. *Geochim Cosmochim Acta* 73:2382-2399

Moretti R, Papale P (2004) On the oxidation state and volatile behaviour in multicomponent gas-melt equilibria. *Chem Geol* 213:265-280

Morizet, Y, Paris M, Gaillard F, Scaillet B (2010) C–O–H fluid solubility in haplobasalt under reducing conditions: An experimental study. *Chem Geol* 279:1-16

Mungall JE (2002) Roasting the mantle: slab melting and the genesis of major Au and Au-rich Cu deposits. *Geology* 30(10): 915-918

Muntean JL, Cline JS, Simon AC, Longo A (2011) Magmatic-hydrothermal origin of Nevada's Carlin-type gold deposits. *Nature Geosci* 4:122-127

Nagashima S, Katsura T (1973) The solubility of sulfur in Na₂O-SiO₂ melts under various oxygen partial pressures at 1100 °C, 1250 °C, and 1300 °C. *B Chem Soc Jpn* 46:3099-3103

Newton RC, Manning CE (2008) Thermodynamics of SiO₂-H₂O fluid near the upper critical end point from quartz solubility measurements at 10kbar. *Earth Planet Sc Lett* 274:241-249

Pallister JS, Hoblitt RP, Meeker GP, Knight RJ, Siems, DF (1996) Magma mixing at Mount Pinatubo: Petrographic and chemical evidence from the 1991 deposits. In: *Fire and Mud: Eruptions and Lahars of Mount Pinatubo, Philippines*

Parkinson IJ, Arculus RJ (1999) The redox state of subduction zones: insights from arc-peridotites. *Chem Geol* 160:409-423

Parkinson IJ, Pearce JA (1998) Peridotites from the Izu-Bonin-Mariana Forearc (ODP Leg 125): Evidence for mantle melting and melt-mantle interaction in a supra-subduction zone setting. *J Petrol* 39:1577-1618.

Parkinson IJ, Arculus RJ, Eggins SM (2003) Peridotite xenoliths from Grenada, Lesser Antilles Island Arc. *Contrib Mineral Petrol* 146(2):241-262

Pistone M, Blundy JD, Brooker RA, (2016) Textural consequences of interaction between hydrous mafic and felsic magmas: an experimental study. *Contrib Mineral Petrol* 171:8, doi 10.1007/s00410-015-1218-4

Pokrovski GS, Dubrovinsky LS (2011) The S₃⁻ ion is stable in geological fluids at elevated temperatures and pressures. *Science* 331:1052-1054

Pawley AR, Holloway JR, McMillan PF (1992) The effect of oxygen fugacity on the solubility of carbon-oxygen fluids in basaltic melt. *Earth Planet Sc Lett* 110, 213-225

Pokrovski GS, Kokh MA, Guillaume D, Borisova AY, Gisquet P, Hazemann J-L, Lahera E, Del Net W, Proux O, Testemale D, Haigis V, Jonchiere R, Seitsonen AP, Ferlat G, Vuilleumier R, Saitta AM, Boiron M-C, Dubessy J (2015) Sulfur radical species form gold deposits on Earth. *Pnatl Acad Sci USA* 112(44) 13484-13489. doi:10.1073/pnas.1506378112

Robie RA, Hemingway BS, Fisher JR (1978) Thermodynamic properties of minerals and related substances at 298.15 K and 1 bar (105 pascals) pressure and at higher temperatures. U.S. Geological Survey; For sale by the Supt. of Docs., U.S. G.P.O., Bulletin 1452, iii, p 456. <http://pubs.usgs.gov/bul/1452/report.pdf>

Samara GA and Giardini AA (1965) Compressibility and electrical conductivity of cadmium sulfide at high pressures. *Phys Rev* 140(1A):A388-A396

Sato K (2012) Sedimentary crust and metallogeny of granitoid affinity: implications from the geotectonic histories of the Circum-Japan sea region, central Andes and Southeastern Australia. *Resour Geol* 62(4):325-351

Scaillet B, Clemente B, Evans BW, Pichavant M (1998) Redox control of sulphur degassing in silicic magmas. *J Geophys Res* 103(B10):23937-23949

Schaaf P, Stimac J, Siebe C, Macias JL (2005). Geochemical evidence for mantle origin and crustal processes in volcanic rocks from Popocatepetl and surrounding monogenetic volcanoes, Central Mexico. *J Petrol* 46:1243-1282

Scott JAJ, Pyle DM, Mather TA, Rose WI (2013) Geochemistry and evolution of the Santiaguito volcanic dome complex, Guatemala. *J Volcanol Geoth Res* 252:92–107.

Sillitoe RH (2012) Copper provinces. Society of Economic Geologists, Special Publications 16:1-18

Sisson TW, Ratajeski K, Hankins WB, Glazner AF (2005) Voluminous granitic magmas from common basaltic sources. *Contrib Mineral Petrol* 148:635–661

Sun W, Arculus RJ, Kamenetsky VS, Binns RA (2004) Release of gold-bearing fluids in convergent margin magmas prompted by magnetite crystallization. *Nature* 431:975-978

Sun W-d, Liang H-y, Ling M-x, Zhan M-z, Ding X, Zhang HZ, Yang X-y, Li Y-l, Ireland TR, Wei Q-r, Fan W-m (2013) The link between reduced porphyry copper deposits and oxidized magmas. *Geochim Cosmochim Acta* 103:263-275

Sverjensky DA, Harrison B, Azzolini D (2014) Water in the deep Earth: the dielectric constant and the solubilities of quartz and corundum to 60kb and 1200°C. *Geochim Cosmochim Acta* 129:125-145

Thibault Y, Holloway JR (1994) Solubility of CO₂ in a Ca-rich leucitite: effects of pressure, temperature and oxygen fugacity. *Contrib Mineral Petrol* 116:216–224.

Ueda A, Itaya T (1981) Microphenocrystic pyrrhotite from dacite rocks of Satsuma-Iwojima, Southwest Kyushu, Japan and the solubility of sulfur in dacite magma. *Contrib Mineral Petrol* 78:21–26

Ulmer P, Luth RW (1991) The graphite-COH fluid equilibrium in P, T, fO₂ space. An experimental determination to 30kbar and 1600°C. *Contrib Mineral Petrol* 106:265-272

Wallace PJ (2005) Volatiles in subduction zone magmas: concentrations and fluxes based on melt inclusion and volcanic gas data. *J Volcanol Geoth Res* 140:217-240

Webster JD, Botcharnikov RE (2011) Distribution of sulfur between melt and fluid in S-O-H-C-Cl-bearing magmatic systems at shallow crustal pressures and temperatures. *Rev Mineral Geochem* 73:247-283

Wilke M, Jugo PJ, Klimm K, Susini J, Botcharnikov R, Kohn SC, Janousch M (2008) The origin of S⁴⁺ detected in silicate glasses by XANES. *Am Mineral* 93: 235–240

Woermann E, Rosenhauer M (1985) Fluid phases and the redox state of the Earth's mantle. Explorations based on experimental, phase-theoretical and petrological data. *Fortschr Mineral* 63(2):263-349

Wood BJ, Virgo D (1989) Upper mantle oxidation state: Ferric iron contents of lherzolite spinel by ^{57}Fe Mössbauer spectroscopy and resultant oxygen fugacities. *Geochim Cosmochim Acta* 53:1277-1291

Wood BJ, Bryndzia LT, Johnson KE (1990) Mantle oxidation state and its relationship to tectonic environment and fluid speciation. *Science* 248: 337-345

Zajacz Z, Candela PA, Piccoli PM, Sanchez-Valle C, Wälle M (2013) Solubility and partitioning behaviour of Au, Cu, Ag and reduced S in magmas. *Geochim Cosmochim Acta* 112:288-304

Zajacz Z (2015) The effect of melt composition on the partitioning of oxidized sulfur between silicate melts and magmatic volatiles. *Geochim Cosmochim Acta* 158:223-224

Zellmer FG, Edmonds M, Straub SM (2014) Volatiles in subduction zone magmatism. Geological Society London, Special Publications. doi 10.1144/SP410.13

Figure Captions

Figure 1: The oxidation states of magmas, their mantle sources and some solid-state buffers. In (a) the fO_2 is shown for a variety of tectonic settings. The main histograms for shallow mantle peridotites are from the dataset of Foley (2011) with additional individual samples from Avachinsky, Arai et al., (2003); Japan-Ichinomegata, Wood and Virgo (1989); Izu-Bonin, Parkinson and Pearce (1998); Cascades, Brandon and Draper, (1996); Grenada, Parkinson et al., (2003); Shiveluch, Bryant et al., (2007); Mexico, Blatter and Carmichael (1998). Redox state of the arc mantle, as implied from geochemical features of lavas, from Mallmann and O'Neill (2009), Lee et al. (2005, 2010) and Evans et al. (2012). Arc basalt range from Carmichael (1991), Eggins (1993), Heath et al. (1998), Macdonald et al. (2000), Hoog et al. (2004), Crabtree and Lange (2011). Specific examples include: Mexico, Carmichael (1991); Shiveluch, Humphreys et al (2006); Grenada, Parkinson et al. (2003). Sulphate-bearing andesites and dacites as listed in Scaillet et al. (1998). MORB range from Christie et al. (1986), Ballhaus et al. (1991), Cottrell and Kelley (2011). In (b) $\log fO_2$ range of various solid-state buffers as a function of temperature and pressure. The upper edge of each range represents 2.0 GPa, the lower edge 0.1 MPa (1 bar). This illustrates the small effect of depth from the top to bottom of the crust. The log unit variation from the Ni-NiO buffer is expressed as ΔNNO and here the 1.0 GPa lines are shown. A typical change from sulphide (S^{2-}) to sulphate (S^{6+}) as a function of fO_2 is shown for the condition 0.2 GPa and 950°C (Botcharnikov et al. 2010) to illustrate the relative scale of this effect.

Figure 2: Secondary (SE) and backscattered (BSE) electron images of run products produced at various pressure, temperature and fO_2 conditions. (a) Experiment at NNO, 1.5GPa and 950°C with garnet (grt) as a main phase and sulphides (sulph) present as $<3 \mu m$ spherical grains in silicate melt and also as inclusions in garnet and amphibole (amph). (b) An example of highly oxidized experiment at NNO+4.7, 1GPa and 841°C showing the presence of anhydrite (anh) and absence of sulphides. (c) Graphite flakes around amphibole agglomerates in reduced NNO-1.5 run at 1.0 GPa and 900°C. Like the COH-fluid, graphite tends to nucleate near crystals or capsule

walls. (d) The decrease in fluid and increase in melt proportions with decreasing temperature for a fixed f_{O_2} and pressure (NNO+2, 1.5GPa). (e) Effect of oxygen fugacity on fluid speciation. CO_2 -rich fluids are stable at $f_{O_2} \geq NNO$ and produce large vesicles $\leq 50 \mu m$ in diameter. In contrast, with graphite present at NNO-1.5 vesicles are $\sim 3 \mu m$ (note change in scale).

Figure 3: Phase relations as a function of oxygen fugacity and temperature for experiments performed at (a) 1.0 and (b) 1.5 GPa. All runs contain fluid and silicate melt. Red line illustrates the transition from CO_2 - H_2O to graphite-COH fluid calculated using Ulmer and Luth (1991). Note that at 1.0 and 1.5 GPa and NNO+2 run products are saturated with pyrrhotite at all temperatures.

Figure 4: Graphic representation of phase proportions demonstrating the effect of temperature and oxygen fugacity on the phase relations in hydrous magmas. Overall, the melt fraction increases with decreasing f_{O_2} owing to the suppression of plagioclase crystallisation and/or the increasing stability of H_2O due to redox reactions.

Figure 5: Bulk starting composition and the range of experimental silicate melts plotted on a total alkali-silica diagram (Le Bas et al. 1986).

Figure 6: Compositional trends for selected components that show distinctive variation with experimental f_{O_2} . Data are presented on an anhydrous basis and presented in wt% and ppm concentrations with $\pm 1\sigma$ uncertainty. Plots of other elements are provided in supplementary materials (Fig.S1).

Figure 7: Ion-probe measurements of water and CO_2 contents in quenched silicate melts as a function of temperature. (a) With decreasing temperature there is a

general increase in dissolved water and decrease in CO₂. Reduced Co-CoO-buffered runs exhibit highest water and lowest CO₂ contents owing to breakdown of CO₂ to graphite+H₂O(±CH₄±CO). (b) A comparison of the volatile contents of fluid-saturated melts in this study and isobars for oxidized (CO₂-H₂O) fluid-saturated melts calculated using the model of Ghiorso and Gualda (2015) at 0.5 and 1.0 GPa. The position of the 1.5 GPa reduced data is discussed in the text.

Figure 8: (a) Sulphur speciation in melt as a function of oxygen fugacity. The modelled speciation includes an intermediate oxidation S-species between S²⁻ and S⁶⁺ transition and is labelled as S⁰. (b) Experimental (symbols) and modelled (grey lines) S-contents in melt for the entire range of studied fO₂. Note that temperature has a strong effect on the Sulphur Content at Anhydride Saturation (SCAS) but only a minor effect on Sulphur Content at Sulphide Saturation (SCSS). The red symbols represent experiments within a narrow temperature range from 841 to 875°C but with unreliable thermocouple readings (see section 2.2). (c) Illustration of the pressure effect on sulphur speciation in Fe-bearing silicate melts expressed as X_{S⁶⁺}. The 0.2 GPa line is based on the basaltic data of Jugo et al. (2010) and Botcharnikov et al. (2011). The 0.5 GPa line is estimated from a single run in this study; the other trachydacite data at 1.0 and 1.5 GPa lines are constructed from the data in (a). With increasing pressure the stability field of sulphide shifts significantly towards more oxidized conditions. It should be noted that the 0.2 GPa/800-1000°C data of Masotta and Keppler (2015) suggest there is a minor effect of melt composition on the estimated position of the S⁶⁺-S²⁻ between basalt, trachyandesite and dacite. This shift is much smaller than the pressure effect illustrated here.

Figure 9: Possible pressure and fO₂ controls on Cu-enrichment in silicate magmas. Grey area delimits the field of graphite saturation at which >80% of CO₂ breaks down to C+H₂O(±CH₄±CO) leading to significant reduction in the amount of exsolved fluid. At fO₂ above the graphite stability field the magmatic fluid is composed mainly of H₂O+CO₂. In relatively 'dry', water under-saturated magmatic systems Cu-enrichment in the absence of sulphide requires very high fO₂ values ΔNNO≥2 at

0.5GPa (mid crust) but an extremely high value $\Delta\text{NNO} \geq 3.5$ (see Fig 1a) towards the deeper crust (or upper mantle) at pressures approaching 1.5 GPa. In contrast, fluid-saturated magmas would facilitate Cu-enrichment at more realistic, $f\text{O}_2$ as sulphur partitioning into exsolving magmatic fluids limits the potential for sulphide saturation and Cu removal.

Figure S1: Composition of silicate melts in experiments performed at 1.0 and 1.5GPa. The values are calculated on anhydrous melt basis and represent mean values of 7-21 analyses; error bars refer to $\pm 1\sigma$ reproducibility.

Figure S2: Calculated values for K_A and K_B constants at 1.0 and 1.5GPa. Whilst K_B mostly controls the position of $X_{S^{6+}}$, K_A determines the position of $X_{S^{2-}}$ and $X_{S_3^-}$ -lines.

Figure S3: Alternative model to Fig. 8, with (a) S-speciation and (b) S-contents in silicate melts at 1.0 GPa assuming the presence of S^{4+} -intermediate species instead of S^0 . Note the maximum for S^{4+} is closer to the oxidized field compared to S^0 (Fig.8). This would limit the stability field of S^{2-} to below $\text{NNO} + 1$ which contradicts the experimental observations.

1 **Table 1** Composition of the starting material (in wt.%).

2

SiO ₂	TiO ₂	Al ₂ O ₃	FeO	Fe ₂ O ₃	MgO	CaO	Na ₂ O	K ₂ O	S ²⁻	SO ₃	Cl	H ₂ O	CO ₂	Total
52.63	1.18	17.13	4.52	2.06	2.71	5.74	4.38	1.74	0.14	0.27	0.15	6.00	1.36	100

3

4 **Table 2** Experimental conditions, composition of fluids and proportions of run
5 products.

6

Pressure, GPa	Temperature, °C	X _{H₂O} in fluid	a _{H₂O}	logfO ₂ ^{ΔNNO}	Run products
Hematite-magnetite buffer					
1.0	841	0.81(2)	0.83	4.77	gl (43.1), fl (2.9), hbl (21.8), plag (27.2), mag (3.6), anh(1.4)
1.0	870	0.78(3)	0.81	4.76	gl (47), fl (2.5), hbl (23.9), plag (23.3), mag (2.1), anh(1.1)
1.0	895	0.80(2)	0.82	4.77	gl (49), fl (2.7), hbl (20.3), plag (23.1), mag (3.5), anh(1.3)
Rhenium-rhenium oxide buffer					
0.5	900	0.79(2)	0.81	1.95	gl (65.2), fl (3), hbl (11.4), plag (17), mag (3.2), anh(0.3)
1.0	850	0.85(2)	0.87	2.21	gl (34.4), fl (3.9), hbl (28.5), plag (31.9), mag (0.6), sulph (0.4)
1.0	900	0.76(2)	0.80	2.06	gl (55.7), fl (2.4), hbl (23.9), plag (16.1), mag (0.7), sulph (0.6)
1.0	950	0.76(2)	0.79	1.98	gl (67.3), fl (2.2), hbl (20.5), plag (9.4), mag (>0.1), sulph (0.6)
1.5	850	0.80(2)	0.83	2.30	gl (46.6), fl (2.5), hbl (30.6), plag (20.3), mag (>0.1), sulph (<0.1)
1.5	900	0.78(4)	0.81	2.19	gl (59.3), fl (2.1), hbl (26), plag (9.8), grt (2.8), sulph (<0.1)
1.5	950	0.70(4)	0.75	2.05	gl (80.3), fl (1), grt (11), cpx (11), sulph (<0.1)
Nickel-nickel oxide buffer					
1.0	850	0.80(5)	0.83	-0.16	gl (49.8), fl (2.8), hbl (26.4), plag (19.4), ilm (0.8), sulph (0.7)
1.0	900	0.75(5)	0.79	-0.21	gl (64.4), fl (1.7), hbl (23.9), plag (8), ilm (0.2), sulph (1)
1.0	950	0.73(5)	0.77	-0.23	gl (83.8), fl (0.8), hbl (13.4), ilm (0.1), sulph (1.9)
1.5	850	0.80(5)	0.83	-0.15	gl (44.4), fl (2.9), hbl (26.6), plag (20.9), grt (4.2), ilm (>0.1), sulph (>0.1), ttn(1)
1.5	900	0.80(5)	0.82	-0.17	gl (67.7), fl (1.3), hbl (21.5), plag (2.6), grt (6.8), sulph (0.1)
1.5	950	0.75(5)	0.79	-0.29	gl (77.3), fl (1), hbl (<0.1), grt (13.9), cpx (7.1), sulph (0.6)
Cobalt-cobalt oxide buffer					
1.0	850	-	0.90	-1.74	gl (75.6), fl (0.7), hbl (21), ilm (0.2), sulph (1), ttn (1.1)
1.0	900	-	0.91	-1.74	gl (74.6), fl (0.7), hbl (21.3), ilm (0.1), sulph (1.6), ttn (1.4), gr
1.0	950	0.75(5)	0.78	-1.53	gl (84), fl (0.2), hbl (15), ilm (0.6), sulph (1)
1.5	850	-	0.91	-1.74	gl (69.7), fl (0.3), hbl (25.5), grt (2.6), ilm (>0.1), sulph (>0.1), ttn(1.3), gr
1.5	900	-	0.91	-1.74	gl (74.5), fl (0.1), hbl (24), sulph (1), ttn(0.4), gr
1.5	950	-	0.91	-1.75	gl (87.9), fl (0.2), cpx (7.7), sulph (3.9), gr

7

8 Quenched glass (gl), fluid (fl), hornblende (hbl), plagioclase (plag), garnet (grt),
9 clinopyroxene (cpx), magnetite (mag), Fe-sulphide (sulph), titanite (ttn),
10 anhydrite (anh).

Table 3 Composition of run products in wt.%, except where indicated.

Phases (#)	SiO ₂	TiO ₂	Al ₂ O ₃	FeO ₁ or Fe (in sulphide)	MgO	CaO	Na ₂ O	K ₂ O	S	Cl	Total	Mg#	H ₂ O	CO ₂	S, ppm
Hematite-magnetite buffer (NNO+4.75)															
<i>1.0GPa, 841°C (+anh)</i>															
Gl(10)	68.58(37)	0.16(2)	17.39(26)	1.63(10)	0.54(6)	2.06(9)	6.11(25)	3.19(11)	0.04(1)	0.26(2)	100.00	0.37	7.22	0.48(12)	387±127
Hbl(8)	40.19(53)	2.70(40)	13.94(23)	13.69(52)	11.75(72)	10.94(13)	3.16(10)	0.72(4)	b.d.l.	b.d.l.	97.09	0.6	7.22	0.48(12)	
Plag(8)	60.31(63)	0.04(3)	24.52(38)	0.58(6)	b.d.l.	6.33(42)	8.27(22)	0.44(3)	b.d.l.	b.d.l.	100.49				
Mag(5)	0.08(3)	15.40(50)	1.18(2)	73.14(56)	1.15(10)	0.11(5)	b.d.l.	b.d.l.	b.d.l.	b.d.l.	91.06				
<i>1.0GPa, 870°C (+anh)</i>															
Gl(10)	66.87(39)	0.28(3)	18.13(22)	2.42(12)	0.55(4)	2.48(4)	5.95(13)	2.98(6)	0.07(1)	0.19(1)	100.00	0.29	7.47(16)	0.53(1)	680±146
Hbl(10)	40.45(69)	2.34(28)	12.87(57)	16.71(42)	10.38(28)	10.49(14)	3.05(8)	0.81(5)	b.d.l.	0.08(1)	97.18	0.53			
Plag(12)	60.29(53)	0.03(1)	25.14(44)	0.50(9)	b.d.l.	6.47(51)	7.93(28)	0.46(6)	b.d.l.	b.d.l.	100.82				
Mag(9)	0.13(3)	24.34(27)	1.05(6)	65.13(34)	1.01(3)	0.15(3)	b.d.l.	b.d.l.	b.d.l.	b.d.l.	91.81				
<i>1.0GPa, 875°C (+anh)</i>															
Gl(13)	67.71(40)	0.21(2)	17.68(19)	2.07(9)	0.70(3)	2.45(6)	5.99(23)	2.88(7)	0.06(1)	0.20(2)	100.00	0.38	6.92(11)	0.52	599±134
Hbl(9)	40.33(66)	2.86(23)	13.90(56)	13.68(69)	11.68(42)	10.89(8)	3.16(8)	0.72(5)	b.d.l.	0.06(1)	97.28	0.6			
Plag(9)	58.83(35)	0.03(2)	25.75(23)	0.55(8)	b.d.l.	7.47(12)	7.57(15)	0.35(2)	b.d.l.	b.d.l.	100.55				
Mag(10)	0.07(2)	14.28(44)	1.36(8)	73.95(38)	1.08(4)	0.09(2)	b.d.l.	b.d.l.	b.d.l.	b.d.l.	90.83				
Rhenium-rhenium oxide buffer (NNO+2)															
<i>0.5GPa, 900°C (+anh)</i>															
Gl(10)	64.00(21)	0.75(3)	18.09(19)	3.70(10)	1.32(6)	3.58(8)	5.85(6)	2.33(8)	0.10(1)	0.18(2)	100.00	0.39	5,87(23)	0.13(1)	1032±137

Hbl(14)	42.78(83)	2.63(40)	10.62(58)	11.91(42)	14.24(56)	11.18(49)	2.67(13)	0.48(4)	b.d.l.	b.d.l.	96.51	0.68			
Plag(4)	51.86(53)	0.29(7)	27.40(91)	1.96(4)	0.57(9)	11.72(49)	2.93(18)	0.69(10)	b.d.l.	0.07(2)	97.49				
Mag(3)	0.55(11)	6.00(12)	4.68(37)	77.77(63)	3.33(19)	0.17(2)	b.d.l.	b.d.l.	b.d.l.	b.d.l.	92.50				
<i>1.0GPa, 850°C</i>															
Gl(8)	67.86(35)	0.31(3)	17.60(9)	2.31(10)	0.36(4)	2.51(8)	5.77(17)	2.97(9)	0.05(1)	0.22(2)	100.00	0.22	7.88(11)	0.47(2)	478±112
Hbl(9)	40.67(41)	2.36(13)	12.67(29)	17.96(43)	9.42(49)	10.57(16)	3.16(10)	0.88(6)	b.d.l.	0.11(1)	97.8	0.48			
Plag(10)	61.61(33)	0.04(1)	24.03(41)	0.47(7)	0.03(1)	5.56(37)	8.62(21)	0.56(9)	b.d.l.	b.d.l.	100.92				
Mag(2)	0.44(40)	29.36(14)	0.77(7)	62.32(55)	0.84(2)	0.1(2)	b.d.l.	0.06(2)	b.d.l.	b.d.l.	93.89				
Sulph(2)	0.21(2)	0.06(1)	0.03(1)	59.91(11)	b.d.l.	0.11(1)	b.d.l.	b.d.l.	37.64(25)	b.d.l.	97.96				
<i>1.0GPa, 900°C</i>															
Gl(9)	64.51(28)	0.47(5)	18.65(19)	3.40(10)	0.65(4)	3.59(6)	5.84(19)	2.58(8)	0.06(1)	0.18(1)	100.00	0.25	7.47(29)	0.59(4)	622±115
Hbl(9)	40.26(70)	2.61(17)	13.71(15)	16.41(44)	10.14(40)	10.71(21)	3.19(8)	0.79(4)	b.d.l.	0.06(1)	97.43	0.52			
Plag(10)	57.72(44)	0.05(2)	26.52(34)	0.54(11)	0.03(3)	8.48(22)	7.06(19)	0.37(9)	b.d.l.	b.d.l.	100.77				
Mag(6)	0.12(8)	30.15(48)	0.99(4)	61.66(58)	1.22(4)	0.15(4)	b.d.l.	b.d.l.	b.d.l.	b.d.l.	94.29				
Sulph(2)	0.22(0)	0.09(1)	0.08(6)	59.95(12)	b.d.l.	0.15(6)	b.d.l.	b.d.l.	37.65(20)	b.d.l.	98.14				
<i>1.0GPa, 950°C</i>															
Gl(10)	62.46(39)	0.63(4)	18.67(16)	4.57(11)	1.08(3)	4.11(7)	5.81(23)	2.30(7)	0.10(1)	0.19	100.00	0.30	6.39(22)	0.56(1)	971±88
Hbl(10)	39.61(60)	2.99(9)	14.86(42)	15.51(37)	10.18(34)	10.63(16)	3.13(6)	0.79(4)	0.03(1)	0.07(1)	97.80	0.54			
Plag(10)	56.97(38)	0.05(4)	26.71(48)	0.59(15)	0.05(5)	8.87(32)	6.84(16)	0.35(9)	b.d.l.	b.d.l.	100.43				
Mag(4)	0.15(5)	28.94(43)	1.23(2)	61.10(62)	1.45(5)	0.17(4)	b.d.l.	0.04(2)	b.d.l.	b.d.l.	93.08				
Sulph(1)	0.18	b.d.l.	0.04	59.78	b.d.l.	0.1	b.d.l.	b.d.l.	37.72	b.d.l.	97.82				
<i>1.5GPa, 850°C</i>															

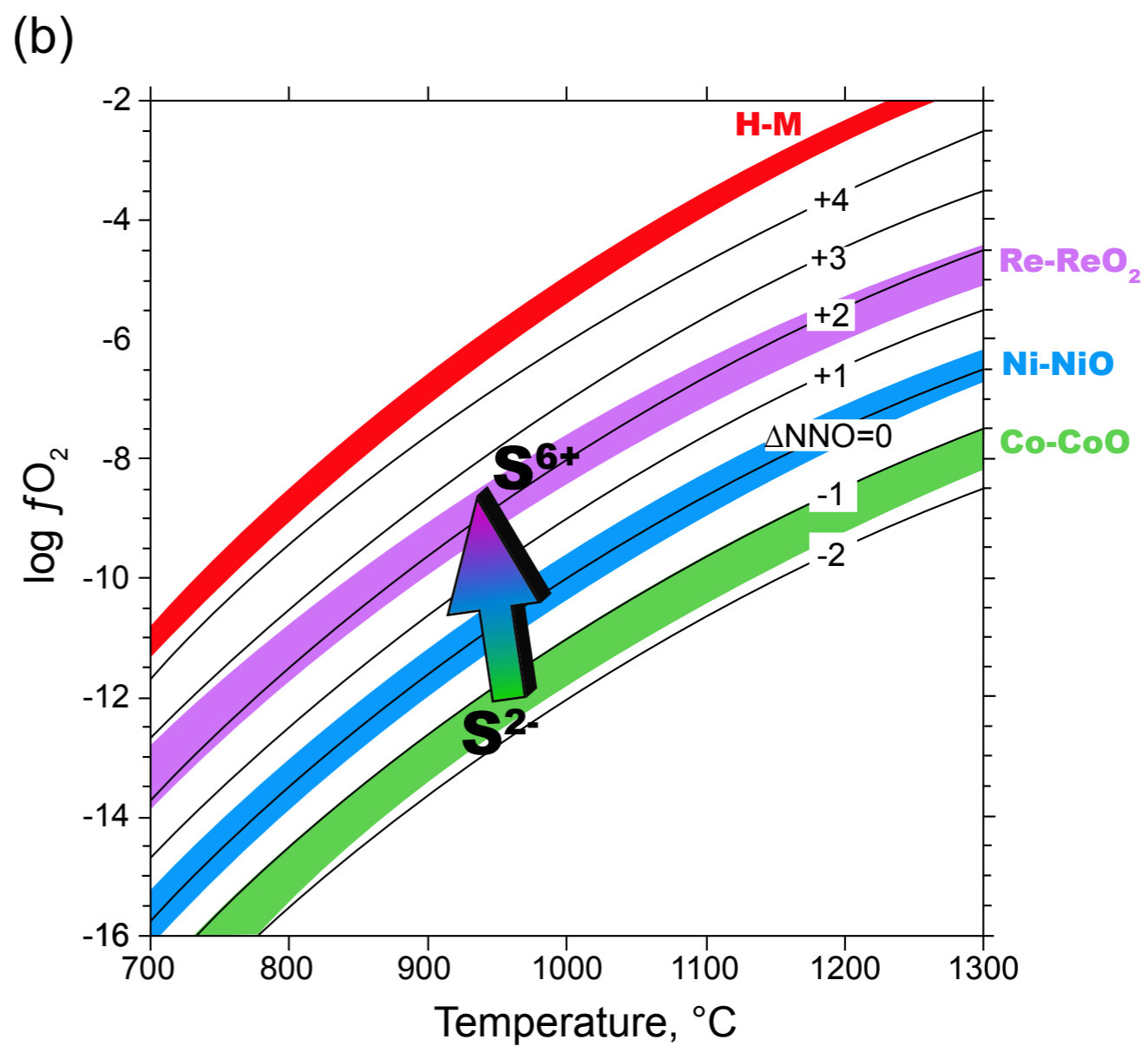
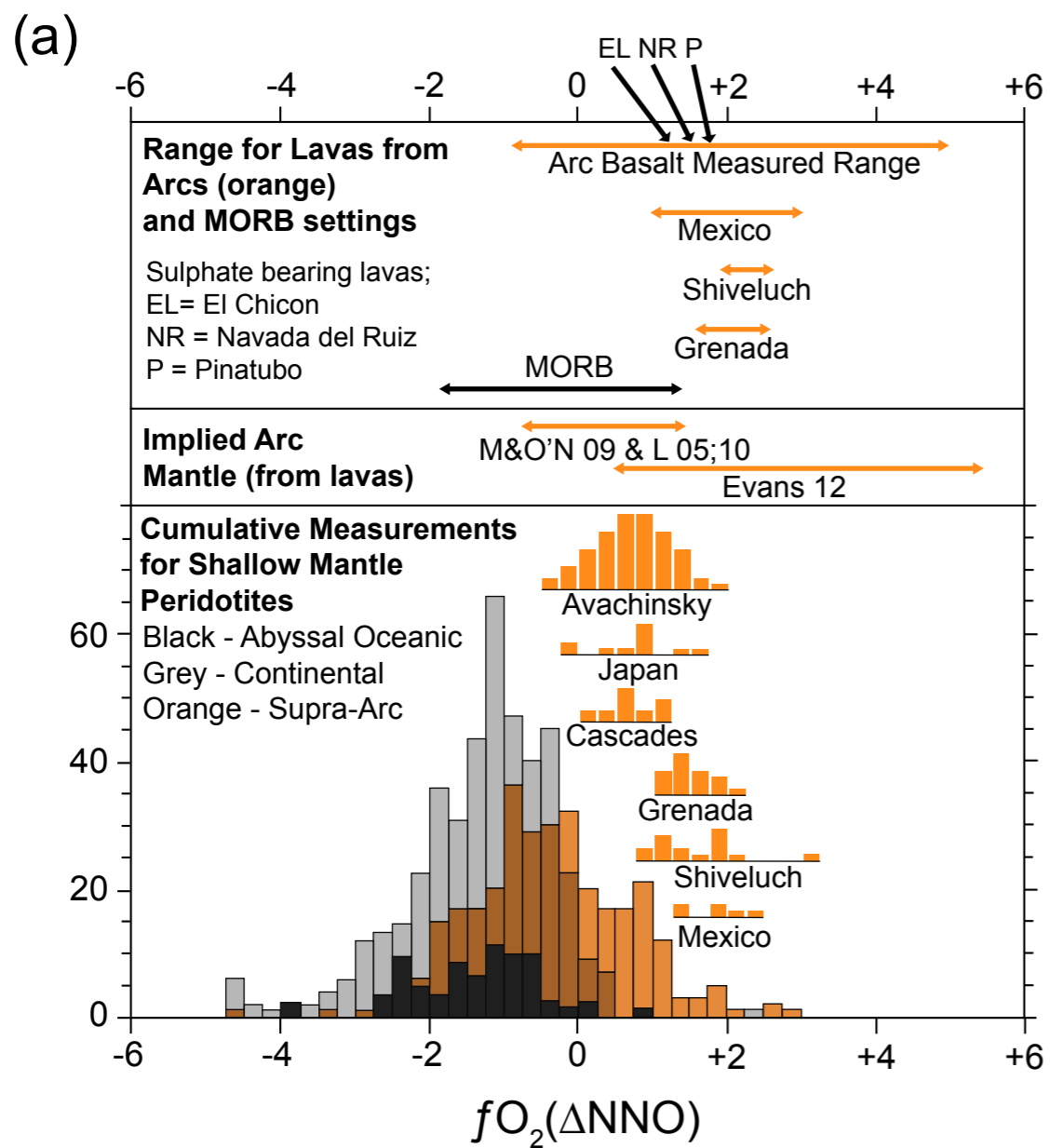
Gl(10)	66.78(18)	0.44(5)	18.10(18)	2.59(13)	0.44(3)	3.01(5)	5.70(8)	2.67(8)	0.05(1)	0.17	100.00	0.24	8.05(7)	0.77(2)	463±93
Hbl(9)	39.32(30)	2.55(32)	15.01(45)	17.97(73)	8.00(34)	9.52(18)	3.00(10)	1.04(4)	0.03(1)	0.10(2)	96.54	0.44			
Plag(11)	60.69(88)	0.03(2)	24.36(59)	0.40(8)	b.d.l.	5.82(62)	7.62(41)	0.44(5)	b.d.l.	b.d.l.	99.36				
Ilm(5)	0.06(2)	40.84(5)	0.67(4)	57.22(12)	1.78(2)	0.09(3)	b.d.l.	b.d.l.	b.d.l.	b.d.l.	100.66				
Sulph(3)	0.15(16)	0.04(1)	b.d.l.	60.04(98)	b.d.l.	0.08(3)	b.d.l.	b.d.l.	39.61	b.d.l.	99.92				
<i>1.5GPa, 900°C</i>															
Gl(10)	65.60(30)	0.55(7)	18.35(17)	3.04(10)	0.66(4)	3.07(5)	6.03(25)	2.47(8)	0.03(1)	0.16(2)	100.00	0.28	7.34(1)	0.96(2)	352±82
Hbl(12)	38.83(22)	3.28(8)	15.62(22)	16.91(34)	8.28(13)	9.44(16)	3.04(7)	0.89(3)	0.04(1)	b.d.l.	96.33	0.47			
Plag(8)	59.52(59)	0.03(1)	25.07(31)	0.4(5)	b.d.l.	6.53(33)	7.29(18)	0.36(2)	b.d.l.	b.d.l.	99.20				
Grt(8)	37.94(27)	1.25(5)	19.92(13)	23.02(17)	6.45(8)	9.89(29)	0.11(2)	b.d.l.	b.d.l.	b.d.l.	98.58	0.33			
Sulph(3)	0.13(12)	0.04(2)	b.d.l.	60.28(21)	b.d.l.	0.1(2)	b.d.l.	b.d.l.	39.36	b.d.l.	99.91				
<i>1.5GPa, 950°C</i>															
Gl(10)	59.95(38)	1.22(12)	18.61(23)	5.77(13)	1.75(6)	4.53(10)	5.77(20)	2.15(6)	0.03(1)	0.17(2)	100.00	0.35	6.81(13)	0.99(10)	338±112
Grt(10)	39.23(21)	1.03(16)	20.91(19)	19.92(31)	10.92(31)	7.35(14)	0.04(2)	b.d.l.	b.d.l.	b.d.l.	99.40	0.49			
Cpx(5)	47.36(35)	1.22(10)	9.41(24)	10.26(53)	10.82(18)	17.38(48)	1.69(4)	0.04(1)	b.d.l.	b.d.l.	98.18	0.65			
Sulph(1)	0.18	0.06	0.04	59.52	b.d.l.	0.19	b.d.l.	b.d.l.	38.2	b.d.l.	98.19				
Nickel-nickel oxide buffer (NNO)															
<i>1.0GPa, 850°C</i>															
Gl(8)	65.74(13)	0.50(2)	18.50(8)	2.63(11)	0.51(2)	3.12(1)	6.07(21)	2.73(9)	0.02(1)	0.17(1)	100.00	0.26	7.76(18)	0.58(1)	164±56
Hbl(10)	41.28(61)	1.94(53)	13.34(97)	16.33(85)	10.34(47)	10.11(30)	3.23(15)	0.73(4)	b.d.l.	0.07(1)	97.37	0.53			
Plag(8)	59.23(82)	0.03(2)	25.52(58)	0.31(6)	b.d.l.	7.08(57)	8.03(25)	0.38(6)	b.d.l.	b.d.l.	100.58				
Ilm(5)	0.51(42)	48.66(31)	0.40(15)	44.29(40)	2.89(8)	0.25(5)	b.d.l.	0.06(2)	b.d.l.	b.d.l.	97.06				
Sulph(4)	0.65(20)	0.13(4)	0.22(14)	62.31(18)	b.d.l.	0.23(9)	b.d.l.	b.d.l.	38.69(11)	b.d.l.	102.05				

<i>1.0GPa, 900°C</i>															
Gl(7)	63.78(29)	0.63(2)	19.11(18)	3.33(9)	0.73(5)	3.94(10)	5.87(19)	2.40(5)	b.d.l	0.19	100.00	0.28	7.79(19)	0.55(1)	(b.d.l)
Hbl(10)	40.47(83)	3.01(31)	14.45(37)	15.26(83)	10.08(60)	10.70(26)	3.06(10)	0.81(7)	b.d.l	0.06(1)	97.9	0,54			
Plag(10)	57.13(66)	0.07(9)	27.02(55)	0.43(15)	0.04(2)	9.01(50)	6.56(37)	0.31(6)	b.d.l	b.d.l	100.57				
Ilm(1)	0.16	49.55	0.35	44.28	3.2	0.21	b.d.l	0.05	b.d.l	b.d.l	97.80				
Sulph(5)	0.25(23)	0.05(2)	b.d.l	60.88(99)	b.d.l	0.11(5)	b.d.l	b.d.l	38.18(114)	b.d.l	99.47				
<i>1.0GPa, 950°C</i>															
Gl(21)	60.59(37)	1.11(4)	19.30(18)	4.24(10)	1.76(7)	5.00(10)	5.66(18)	2.11(6)	0.02(1)	0.19(1)	100.00	0.42	7.40(8)	0.64	217±97
Hbl(11)	41.39(67)	2.79(53)	14.69(66)	11.26(70)	12.94(70)	10.76(36)	3.05(10)	0.72(6)	b.d.l	0.05(1)	97.65	0.67			
Ilm(1)	0.48	50.68	0.56	39.4	6.19	0.56	0.11	0.04	b.d.l	b.d.l	98.02				
Sulph(4)	0.28(2)	0.09(1)	0.09(6)	60.95(51)	b.d.l	0.17(3)	b.d.l	b.d.l	36.72(19)	b.d.l	98.30				
<i>1.5GPa, 850°C</i>															
Gl(13)	68.57(25)	0.35(2)	17.80(16)	1.99(10)	0.31(2)	2.42(5)	5.63(14)	2.71(10)	0.01(1)	0.21(2)	100.00	0.22	8.26(11)	0.67(2)	116±59
Hbl(9)	39.71(56)	2.62(38)	14.81(61)	18.79(76)	7.26(53)	9.41(36)	3.07(13)	0.96(8)	b.d.l	0.14(2)	97.77	0.41			
Plag(9)	61.06(50)	0.04(3)	24.06(60)	0.32(6)	b.d.l	5.42(54)	8.02(32)	0.44(9)	b.d.l	b.d.l	99.36				
Grt(3)	37.57(53)	1.24(26)	20.39(38)	23.36(55)	4.16(14)	12.06(59)	0.14(1)	b.d.l	b.d.l	b.d.l	98.92	0.24			
Ilm(1)	0.21	51.4	0.34	42.02	1.97	0.27	b.d.l	b.d.l	b.d.l	b.d.l	96,21				
Sulph(1)	0.29	0.04	0.08	61.48	b.d.l	0.08	b.d.l	b.d.l	38.21	b.d.l	100.18				
Ttn(3)	30.19(5)	35.98(19)	2.33(20)	0.97(8)	b.d.l	28.00(21)	b.d.l	0.06(2)	b.d.l	b.d.l	97.53				
<i>1.5GPa, 900°C</i>															
Gl(10)	64.74(16)	0.71(3)	18.99(23)	2.75(10)	0.74(4)	3.43(6)	6.02(10)	2.41(5)	0.02(1)	0.18(2)	100.00	0.32	7.42(38)	0.92(8)	188±135
Hbl(5)	39.17(64)	3.35(34)	16.31(53)	15.76(76)	8.48(65)	10.00(21)	3.06(14)	0.93(7)	b.d.l	0.09(1)	97.15	0.49			

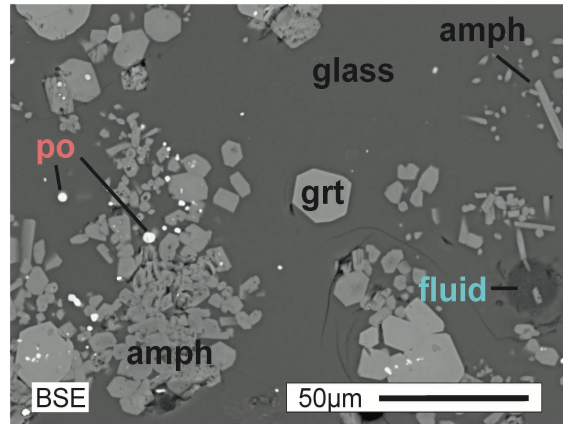
Plag(5)	58.24(30)	b.d.l	25.78(35)	0.35(10)	b.d.l	7.43(23)	6.76(10)	0.34(9)	b.d.l	b.d.l	98.90				
Grt(9)	37.93(29)	1.52(13)	20.57(23)	21.90(52)	6.26(27)	10.74(43)	0.12(2)	b.d.l	b.d.l	b.d.l	99.04	0.34			
Sulph(1)	0.57	0.16	0.35	60.9	b.d.l	0.15	b.d.l	0.06	38.42	b.d.l	100.61				
<i>1.5GPa, 950°C</i>															
Gl(10)	62.18(25)	1.12(4)	19.16(21)	3.61(10)	1.34(5)	4.18(8)	5.99(11)	2.21(10)	0.02(1)	0.18(1)	100.00	0.4	7.43(8)	1.07(9)	191±112
Hbl(4)	39.78(42)	3.44(39)	16.21(76)	12.91(55)	10.67(65)	9.83(17)	3.05(22)	0.81(4)	b.d.l	0.08(0)	96.87	0.6			
Grt(17)	38.53(26)	1.39(17)	21.13(28)	20.65(33)	8.66(30)	9.21(22)	0.09(4)	b.d.l	b.d.l	b.d.l	99.66	0.43			
Cpx(5)	47.91(53)	1.16(17)	8.62(63)	10.73(99)	10.90(90)	17.58(90)	1.93(17)	0.05(5)	b.d.l	b.d.l	98.88	0.64			
Sulph(1)	0.25	0.11	b.d.l	61.38	b.d.l	0.3	b.d.l	b.d.l	38.31	b.d.l	100.35				
Cobalt-cobalt oxide buffer (NNO-1.7)															
<i>1.0GPa, 850°C</i>															
Gl(9)	64.52(24)	0.49(2)	19.94(13)	2.40(12)	0.62(5)	4.25(7)	5.53(12)	2.25(8)	0.03(1)	0.16(2)	100.00	0.28	9.48(43)	0.33(9)	277±122
Hbl(8)	42.58(84)	1.91(24)	13.84(75)	13.48(80)	12.38(49)	10.56(42)	3.02(10)	0.63(2)	b.d.l	0.03(2)	98.43	0.62			
Ilm(7)	0.18(7)	50.31(84)	0.23(3)	43.24(27)	3.01(9)	0.18(5)	b.d.l	b.d.l	b.d.l	b.d.l	97.15				
Sulph(4)	0.45(33)	0.08(1)	0.16(11)	62.24(29)	b.d.l	0.21(10)	b.d.l	b.d.l	37.76(30)	b.d.l	100.9				
Ttn(1)	31.6	36.7	2.6	0.9	0.1	27.6	b.d.l	b.d.l	b.d.l	b.d.l	99.5				
<i>1.0GPa, 900°C (+gr)</i>															
Gl(8)	63.81(28)	0.62(3)	20.09(29)	2.17(12)	0.74(2)	4.30(8)	5.79(14)	2.27(6)	0.02(1)	0.17(2)	100.00	0.34	8.99(14)	0.23(1)	208±109
Hbl(6)	42.29(82)	2.36(92)	13.89(33)	13.05(92)	12.44(93)	10.26(68)	3.20(8)	0.66(7)	b.d.l	0.05(1)	98.29	0.63			
Ilm(1)	0.48	51.06	0.39	40.62	4.64	0.23	0.1	0.07	b.d.l	b.d.l	97.59				
Sulph(3)	0.07(6)	b.d.l	b.d.l	63.17(22)	b.d.l	0.08	0.06(1)	b.d.l	38.29(2)	b.d.l	101.67				
Ttn(5)	30.69(75)	36.10(57)	2.37(27)	0.50(70)	0.09(2)	27.55(16)	0.05(2)	0.05(2)	b.d.l	b.d.l	97.35				

<i>1.0GPa, 950°C</i>															
Gl(11)	60.85(23)	0.91(2)	20.52(20)	3.42(13)	0.98(4)	5.11(9)	5.77(14)	2.21(7)	0.02(1)	0.20(1)	100.00	0.34	8.44(14)	0.57(2)	166±100
Hbl(7)	40.46(40)	3.01(64)	15.97(55)	10.54(32)	12.72(31)	11.00(24)	3.17(4)	0.78(3)	b.d.l.	0.04(1)	97.69	0.68			
Ilm(2)	0.78(40)	49.3(40)	0.6(14)	42.09(13)	4.10(27)	0.43(6)	0.09(3)	0.07	b.d.l.	b.d.l.	97.46				
Sulph(4)	0.80(73)	0.10(3)	0.32(31)	61.50(44)	b.d.l.	0.24(10)	b.d.l.	b.d.l.	37.47(52)	b.d.l.	100.43				
<i>1.5GPa, 850°C (+gr)</i>															
Gl(10)	66.09(25)	0.41(3)	19.39(13)	1.85(11)	0.45(4)	3.37(5)	5.88(16)	2.32(5)	0.03(1)	0.18(2)	100.00	0.3	9.31(3)	0.10	258±113
Hbl(7)	39.76(49)	2.95(11)	15.87(52)	17.28(88)	7.34(35)	9.86(23)	3.16(12)	0.97(5)	b.d.l.	0.13(2)	97.32	0.43			
Grt(8)	38.00(18)	1.53(16)	20.63(42)	20.96(79)	4.44(29)	13.42(53)	0.12(3)	b.d.l.	b.d.l.	b.d.l.	99.10	0.27			
Ilm(2)	b.d.l.	50.93(38)	0.39(6)	41.91(3)	2.76	0.97(13)	b.d.l.	b.d.l.	b.d.l.	b.d.l.	96.96				
Sulph(3)	0.12(6)	0.06(3)	0.05(3)	62.03(30)	b.d.l.	0.11(3)	b.d.l.	b.d.l.	38.13	b.d.l.	100.50				
Ttn(4)	30.46(20)	35.73(44)	2.67(27)	0.96(5)	0.05(3)	27.92(9)	0.04(3)	0.07(3)	b.d.l.	b.d.l.	97.92				
<i>1.5GPa, 900°C (+gr)</i>															
Gl(10)	62.24(19)	0.73(2)	19.81(25)	2.32(10)	0.80(7)	3.98(12)	5.65(10)	2.25(7)	0.03(1)	0.17(1)	100.00	0.38	9.26(32)	0.14(1)	287±138
Hbl(9)	39.16(62)	3.44(19)	17.56(33)	13.95(99)	9.19(63)	10.58(22)	3.09(9)	1.03(4)	0.04(1)	0.08(1)	98.12	0.54			
Sulph(6)	0.34(10)	0.08(3)	0.09(2)	61.87(19)	b.d.l.	0.18(3)	b.d.l.	b.d.l.	38.26(31)	b.d.l.	100.82				
Ttn(1)	31.54	35.62	3.03	0.84	0.1	27	0.28	0.16	b.d.l.	b.d.l.	98.57				
<i>1.5GPa, 950°C (+gr)</i>															
Gl(10)	61.83(29)	1.28(3)	20.01(18)	1.85(5)	2.36(8)	5.00(9)	5.40(16)	2.03(7)	0.04(1)	0.15(2)	100.00	0.70	8.49(28)	0.21(1)	399±61
Cpx(9)	50.45(32)	0.9(12)	6.55(69)	7.86(89)	13.49(49)	18.83(59)	1.32(16)	0.05(2)	b.d.l.	b.d.l.	99.45	0.75			
Sulph(4)	0.22(5)	0.07(2)	0.05(1)	61.66(24)	b.d.l.	0.17(4)	b.d.l.	b.d.l.	38.39(12)	b.d.l.	100.56				

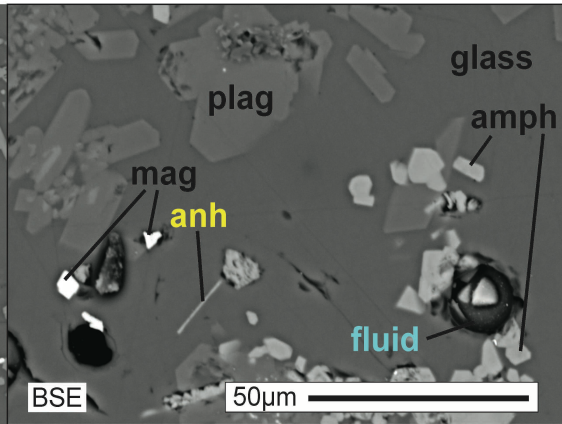
Composition of quenched glasses (gl) is presented as anhydrous normed to 100wt.%. Anhydrite analyses are not present due to interferences caused by neighbored crystals and melt during analyses (see text). Detailed concentrations of S in glass in ppm are given on the right side.



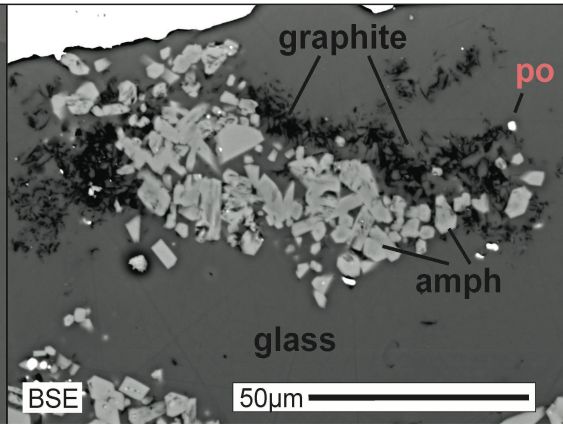
(a) NNO, 950°C, 1.5 GPa



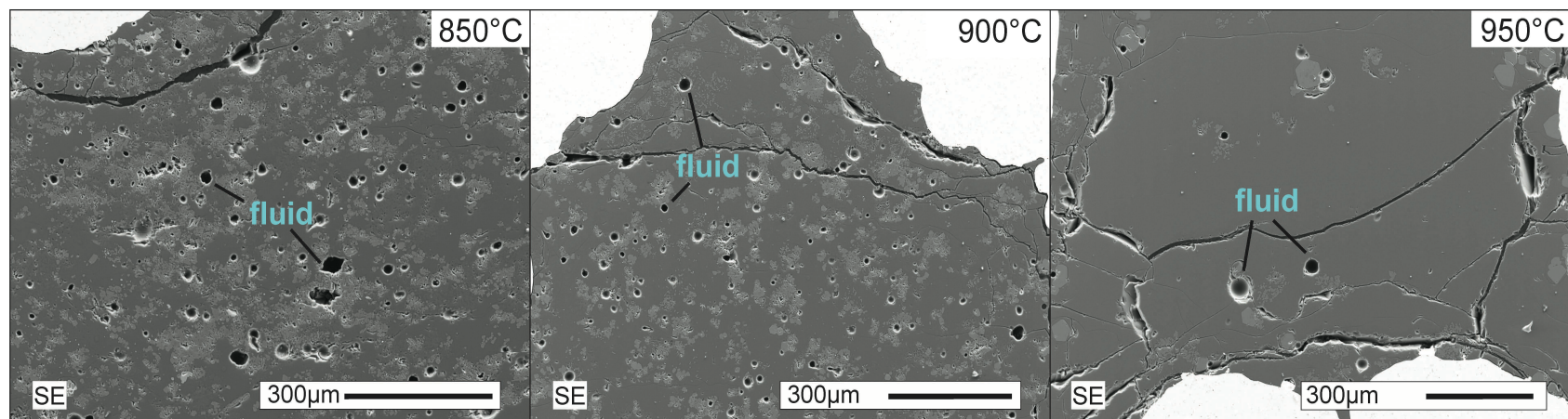
(b) NNO+4.7, 841°C, 1.0 GPa



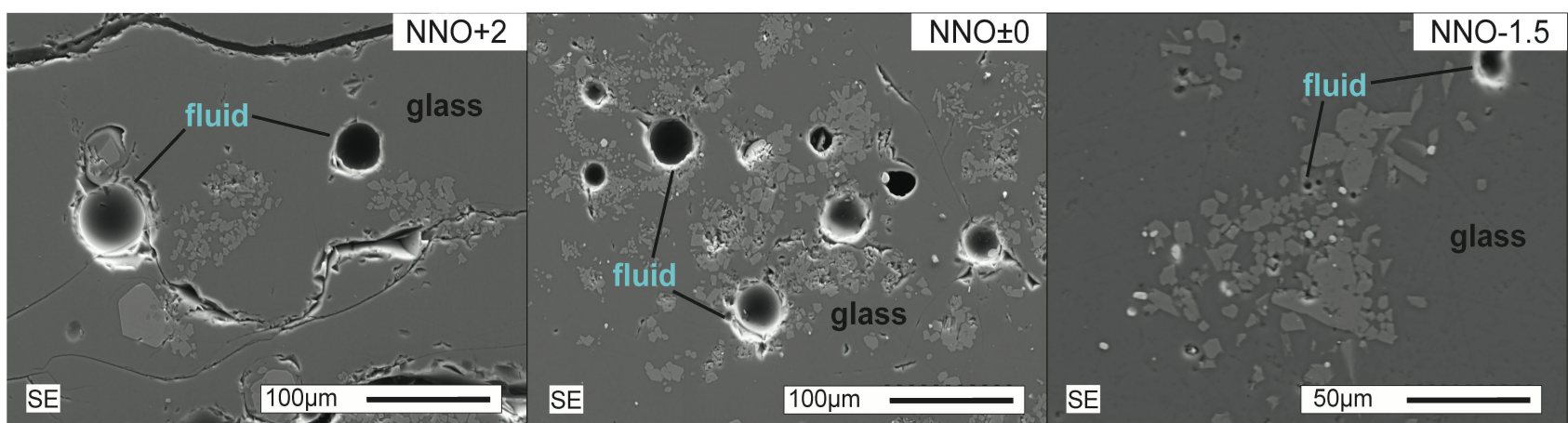
(c) NNO-1.5, 900°C, 1.0 GPa

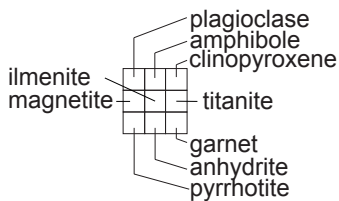
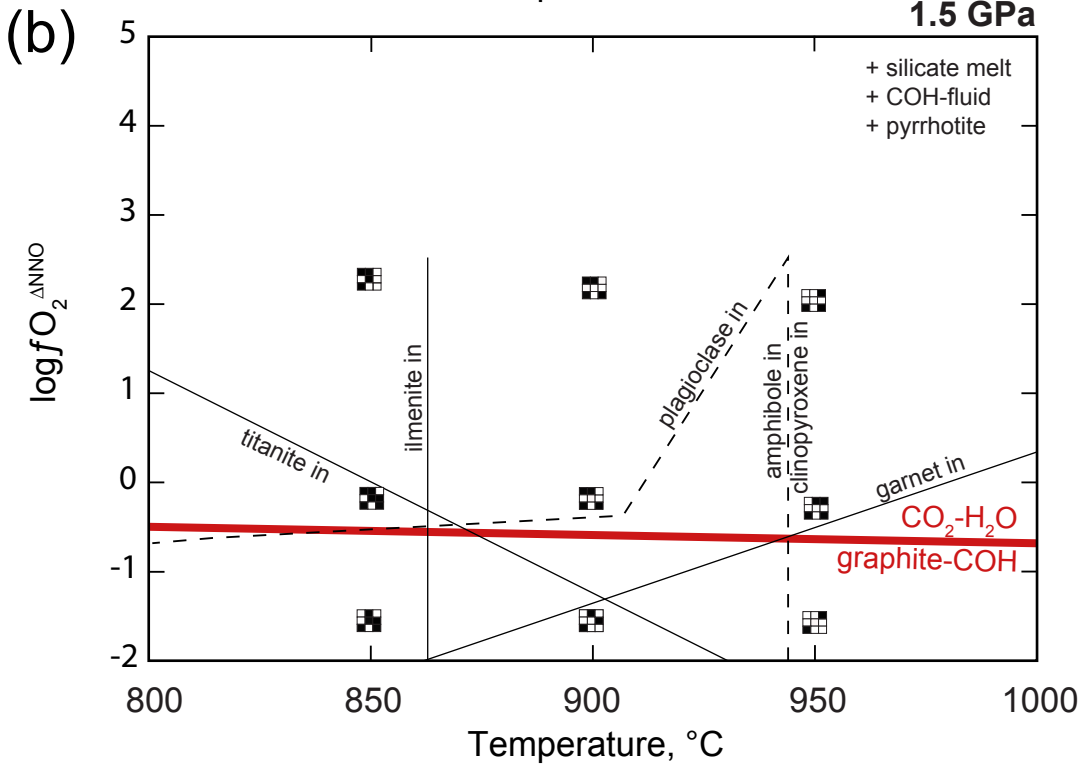
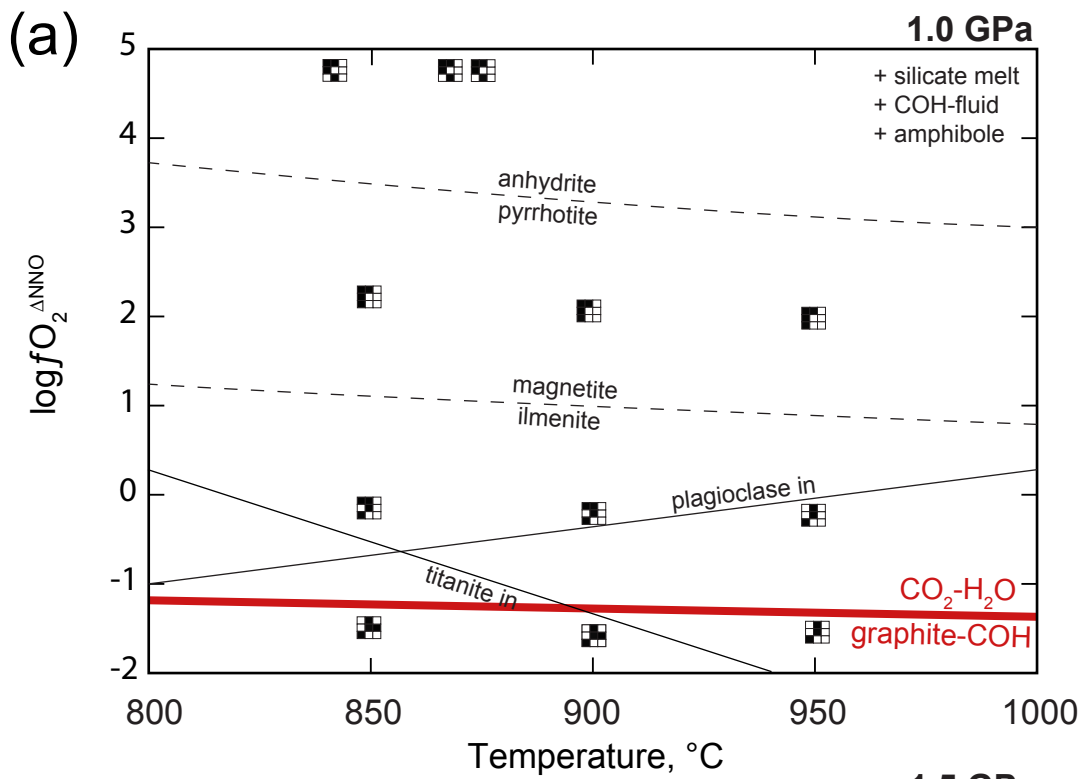


(d) NNO+2, 1.5 GPa



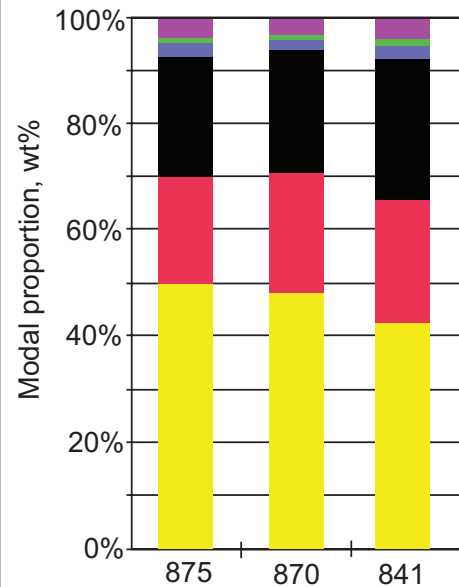
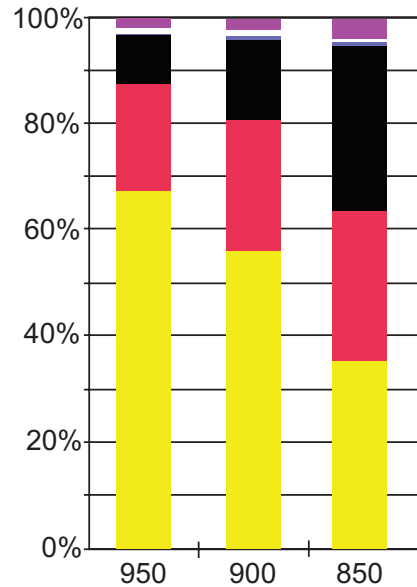
(e) 950°C, 1.5 GPa



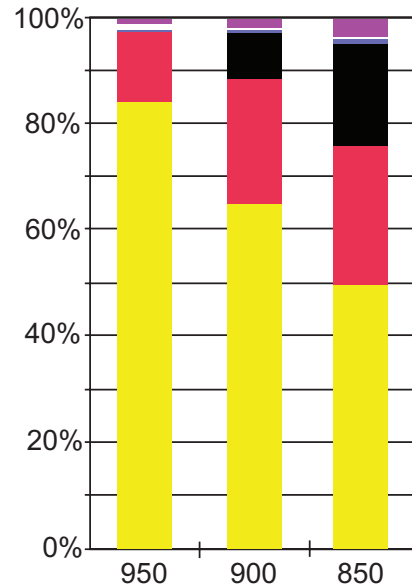


1.0GPa

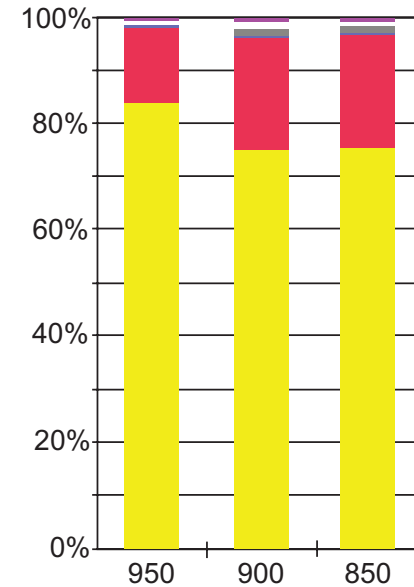
Hematite-Magnetite

Re-ReO₂

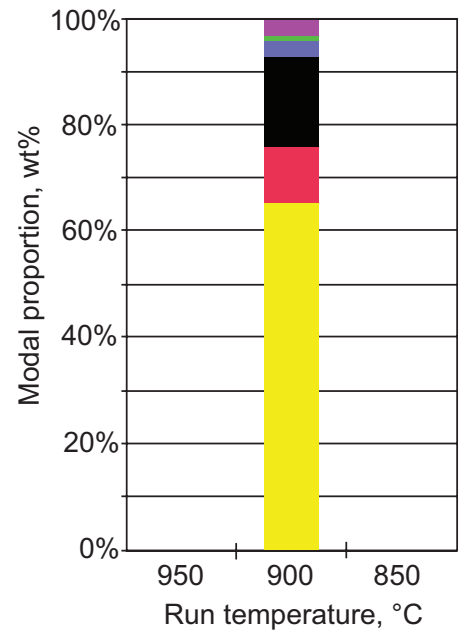
Ni-NiO



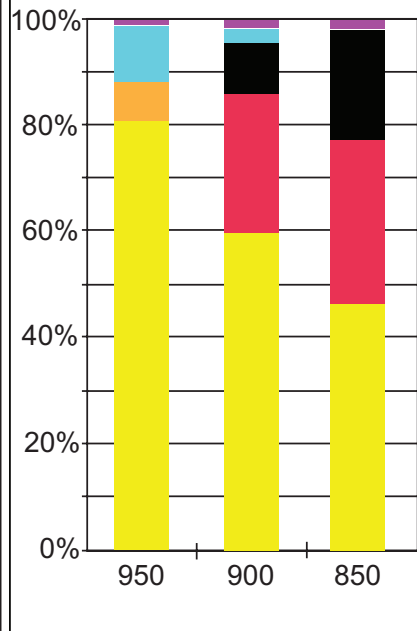
Co-CoO



Run temperature, °C

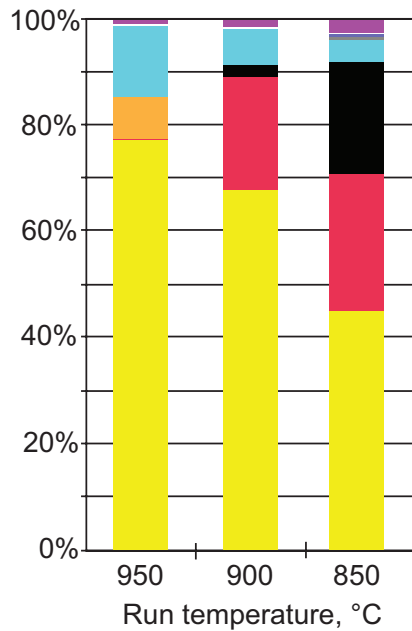
0.5GPaRe-ReO₂

Run temperature, °C

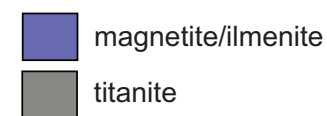
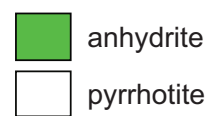
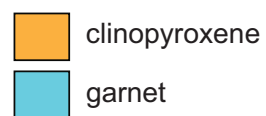
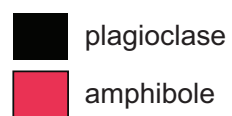
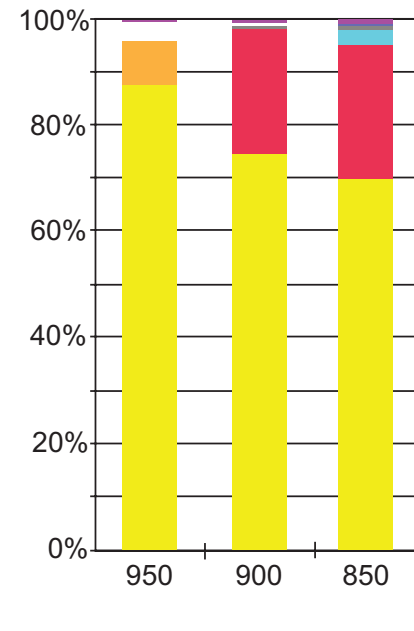
1.5GPaRe-ReO₂

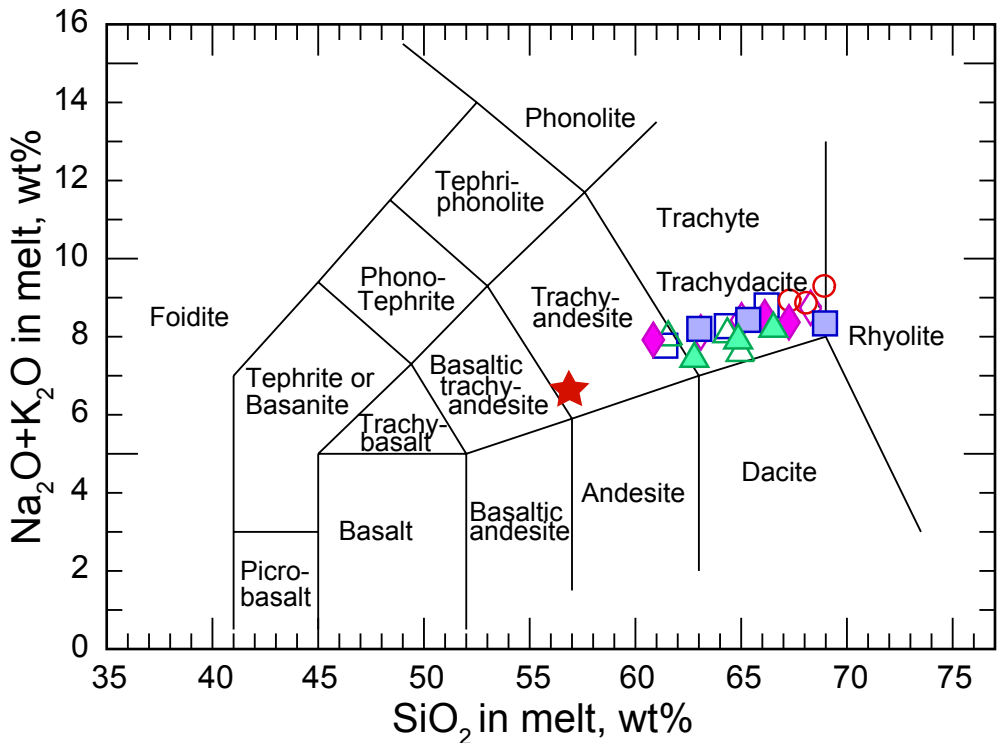
Run temperature, °C

Ni-NiO



Co-CoO

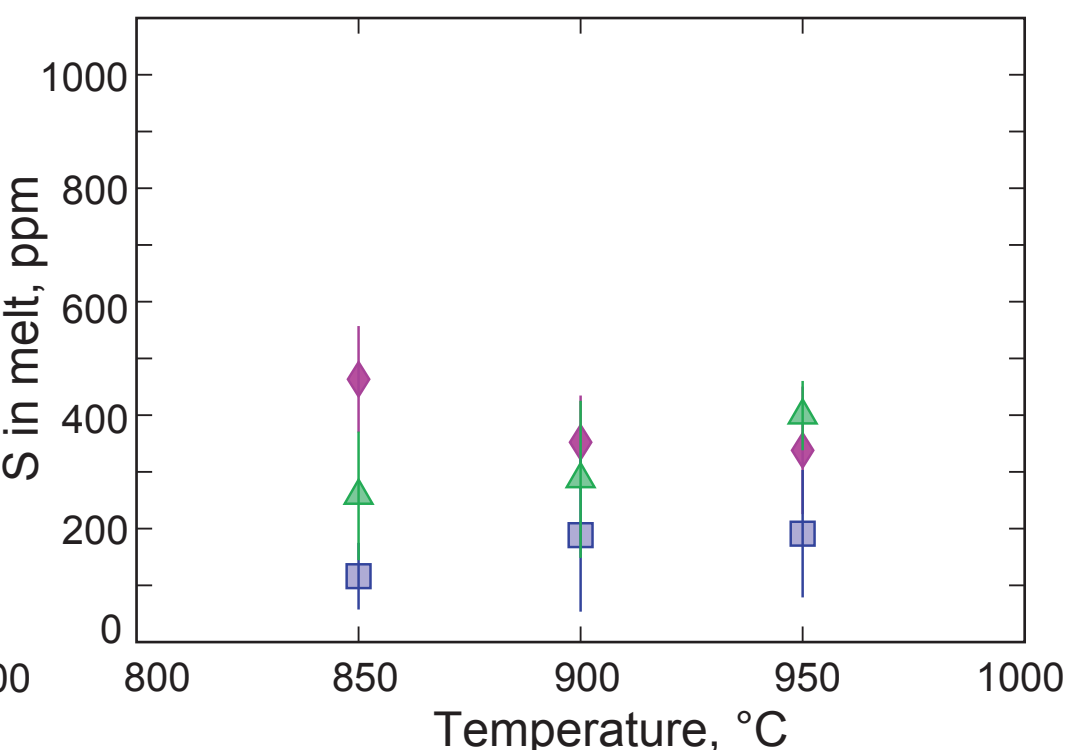
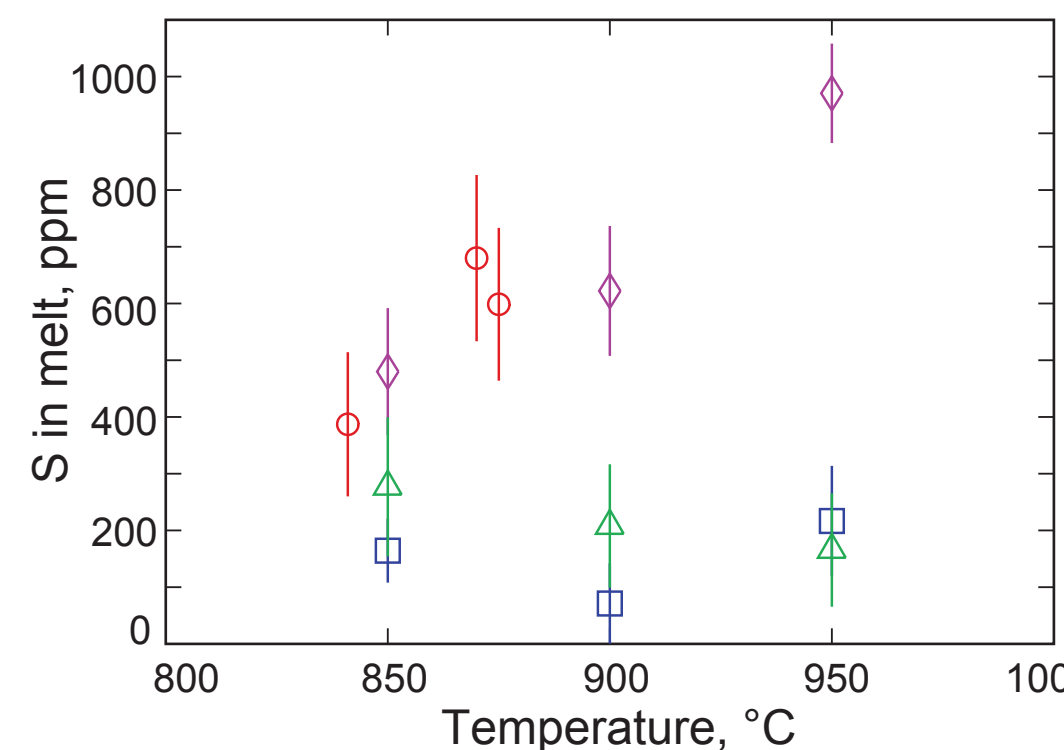
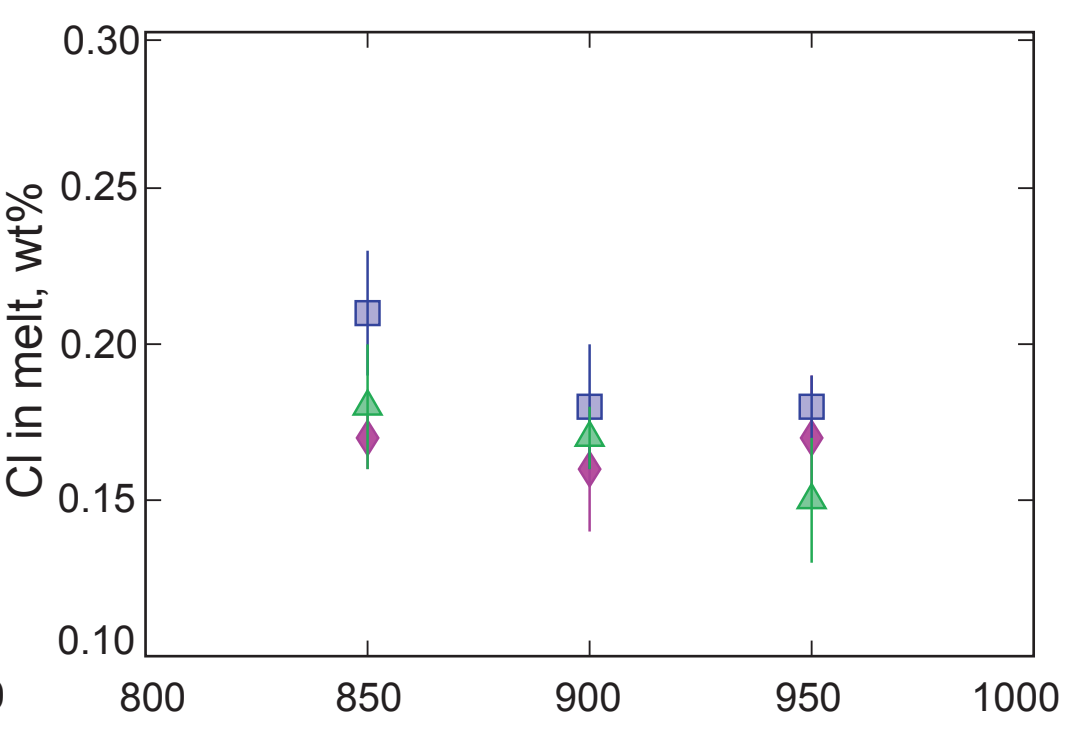
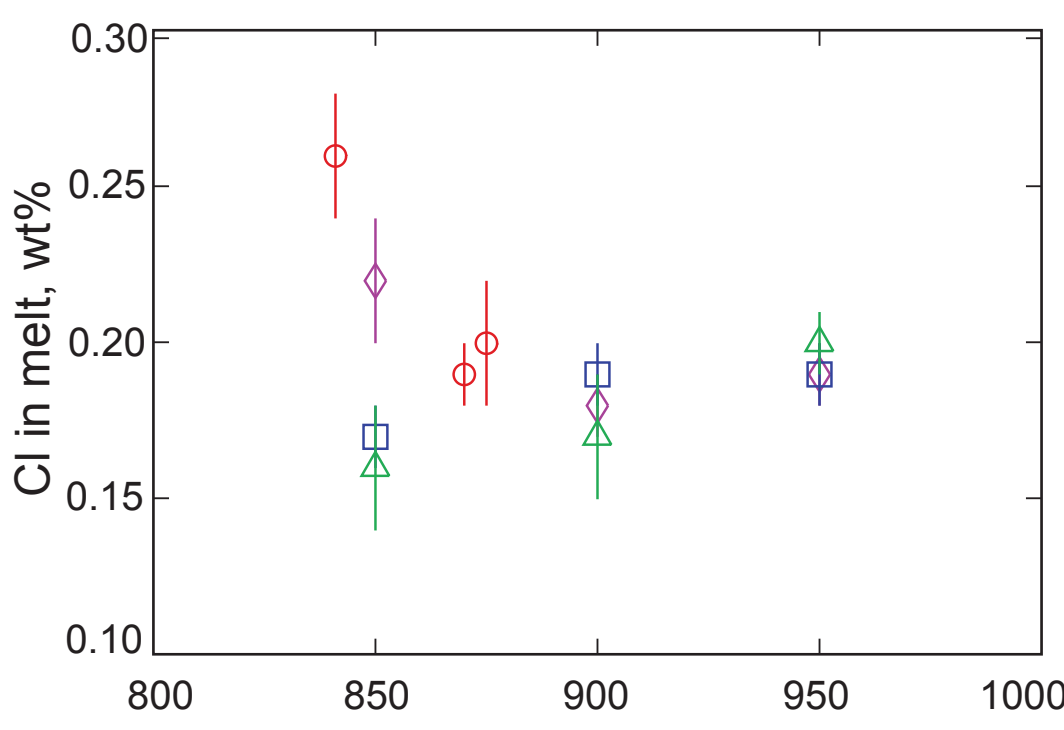
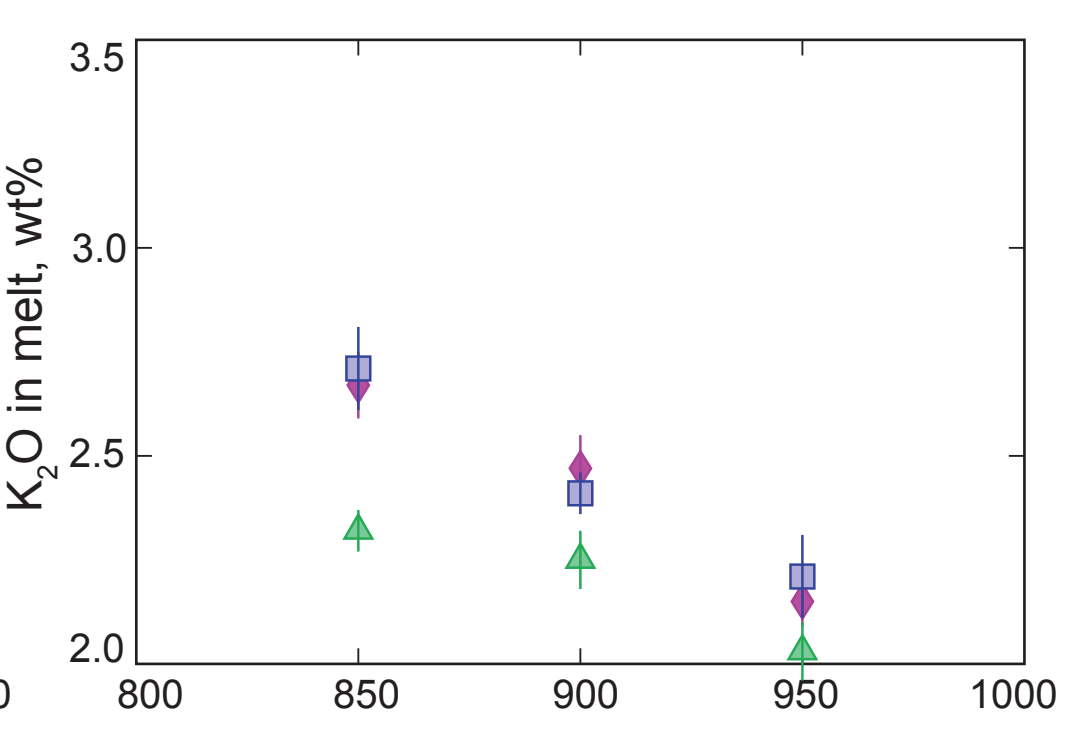
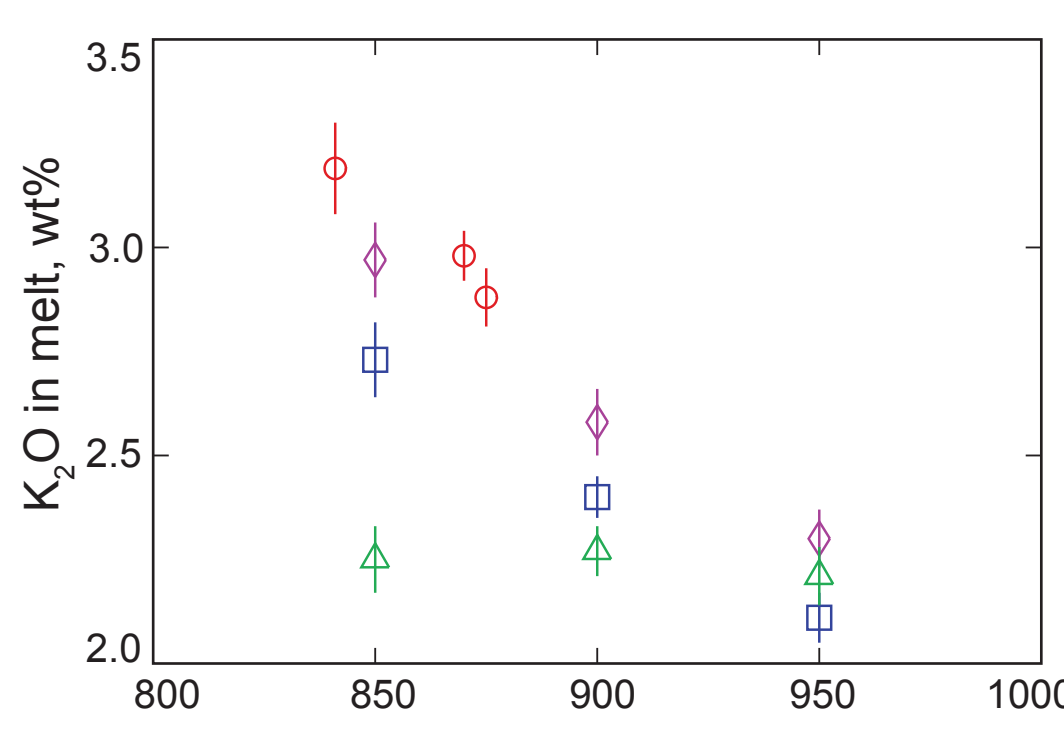
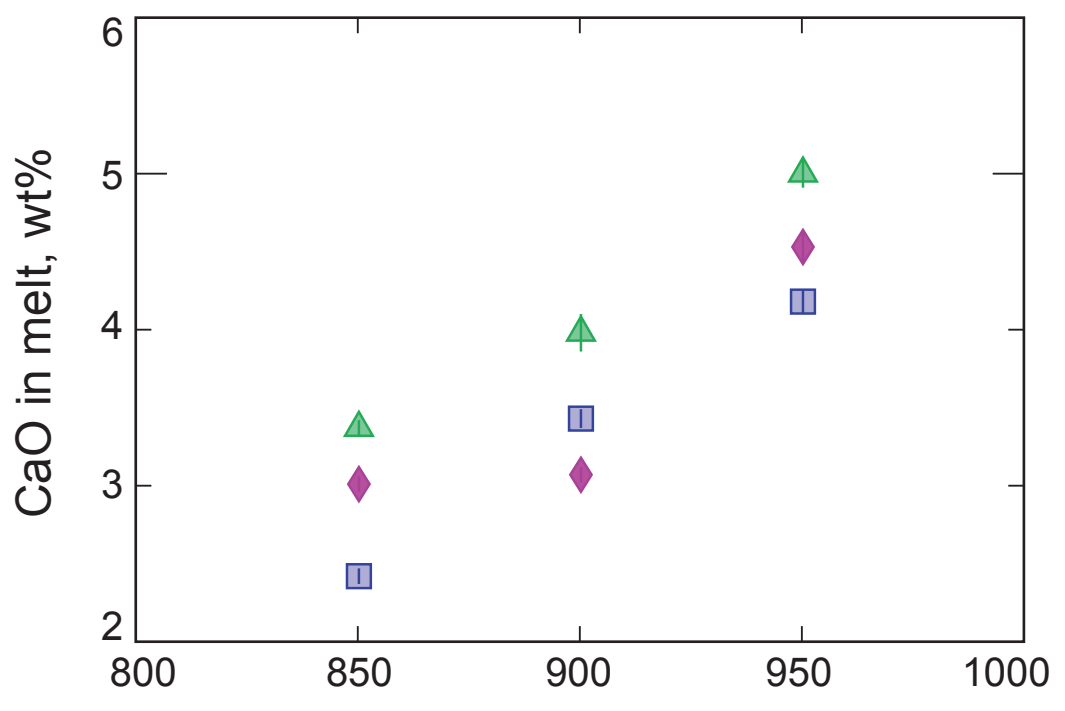
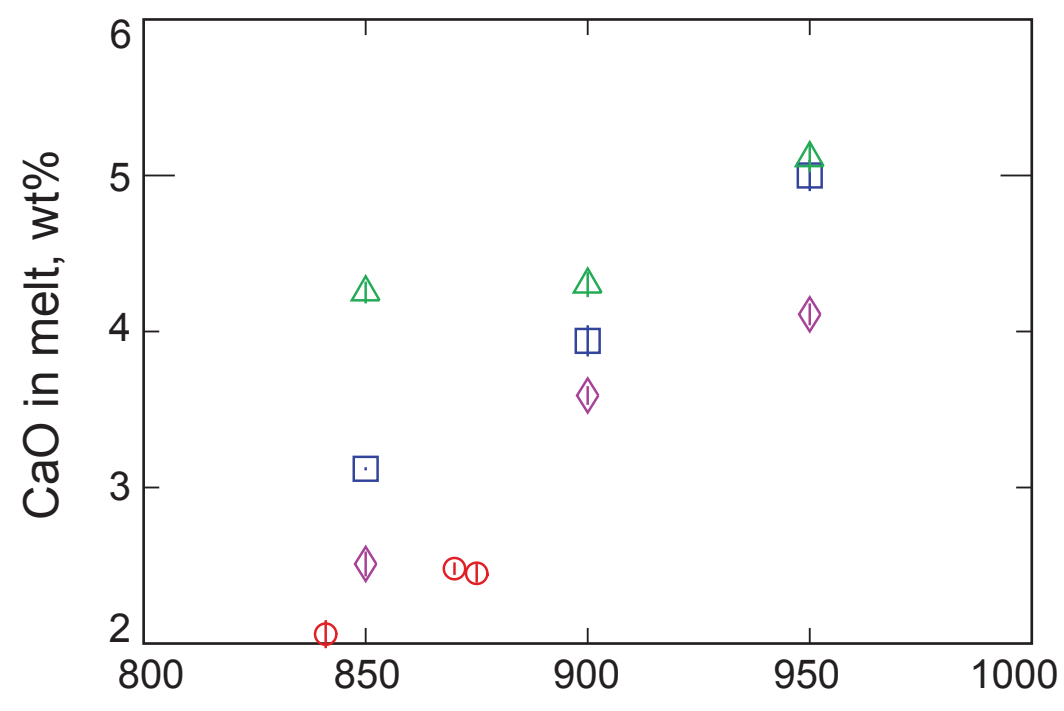
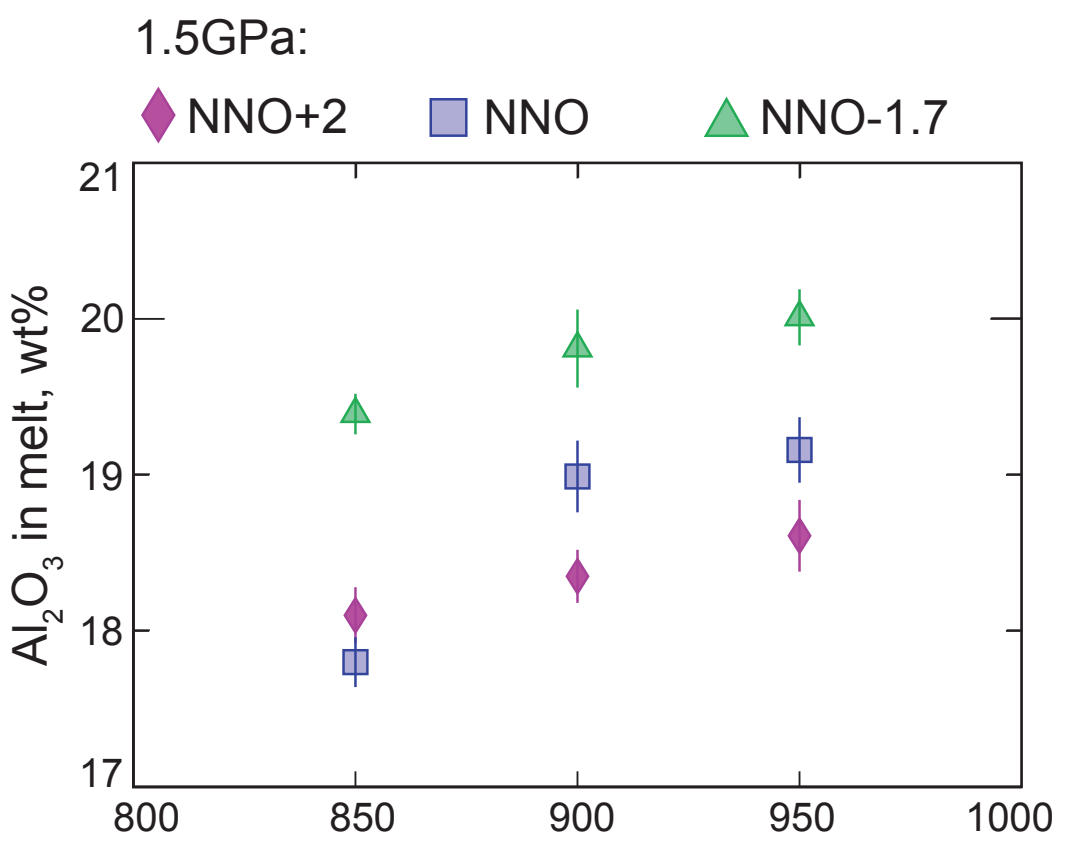
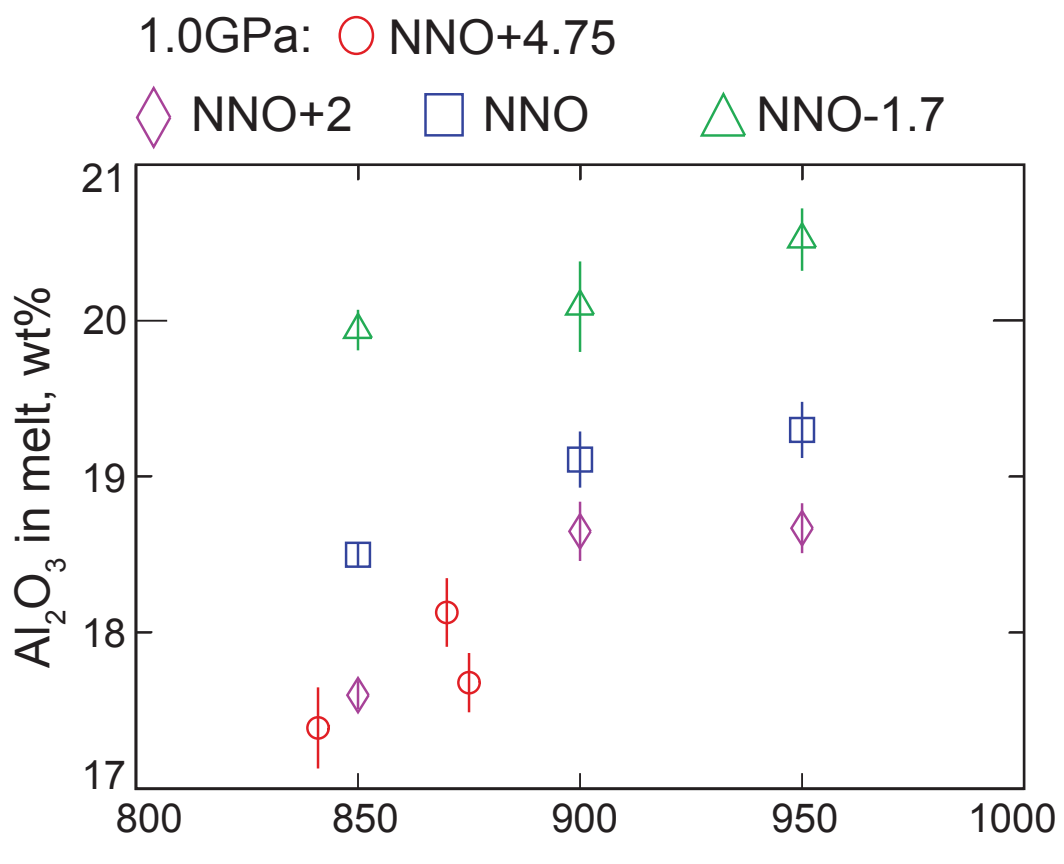


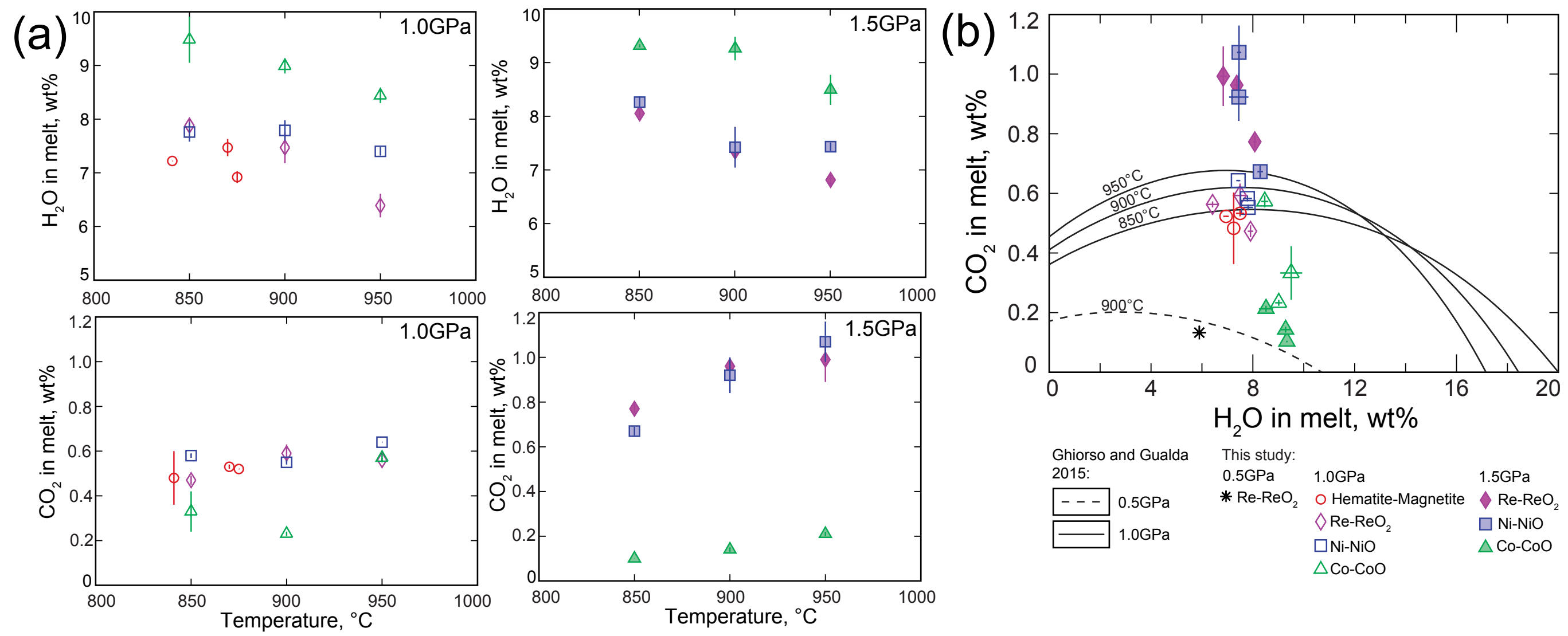


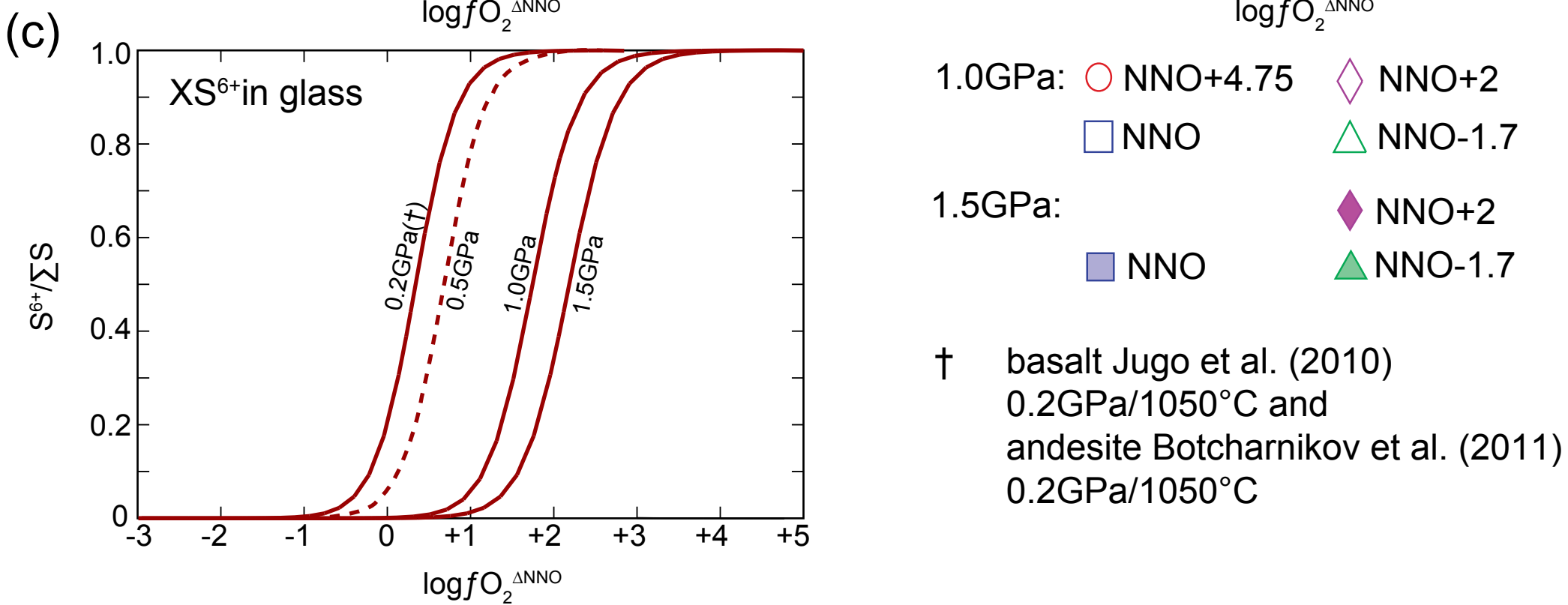
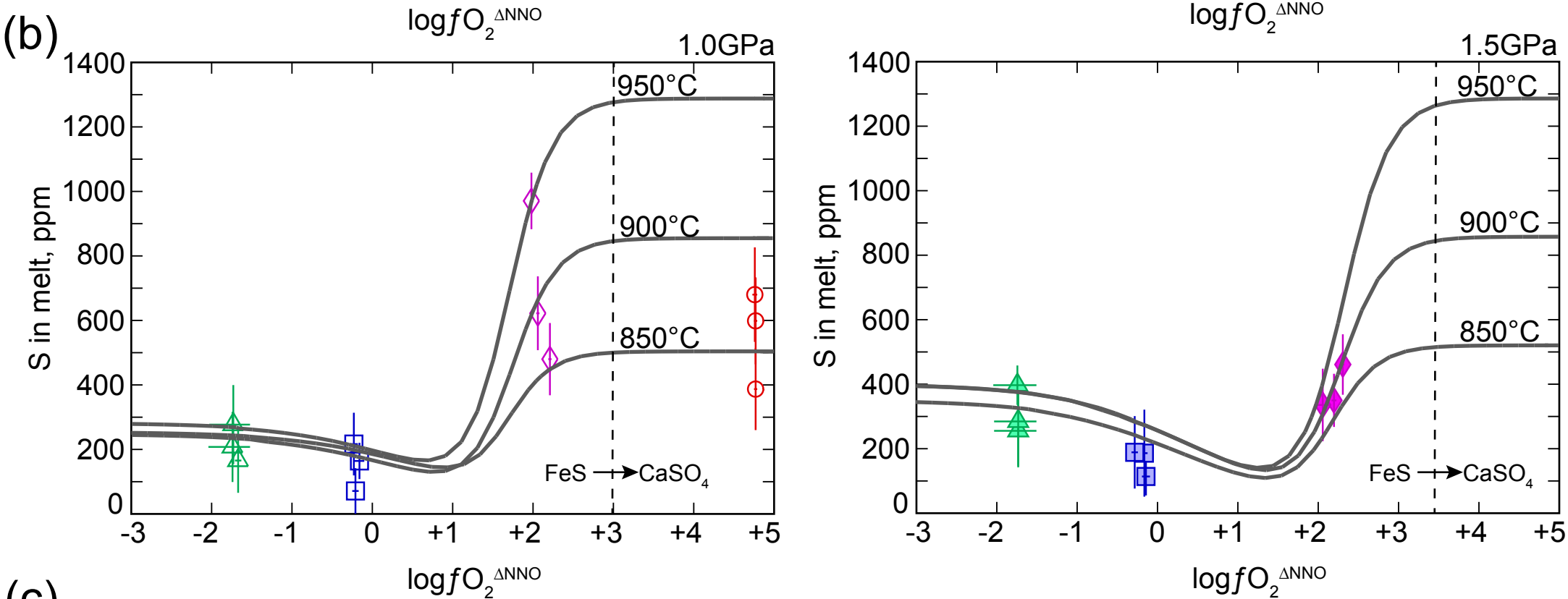
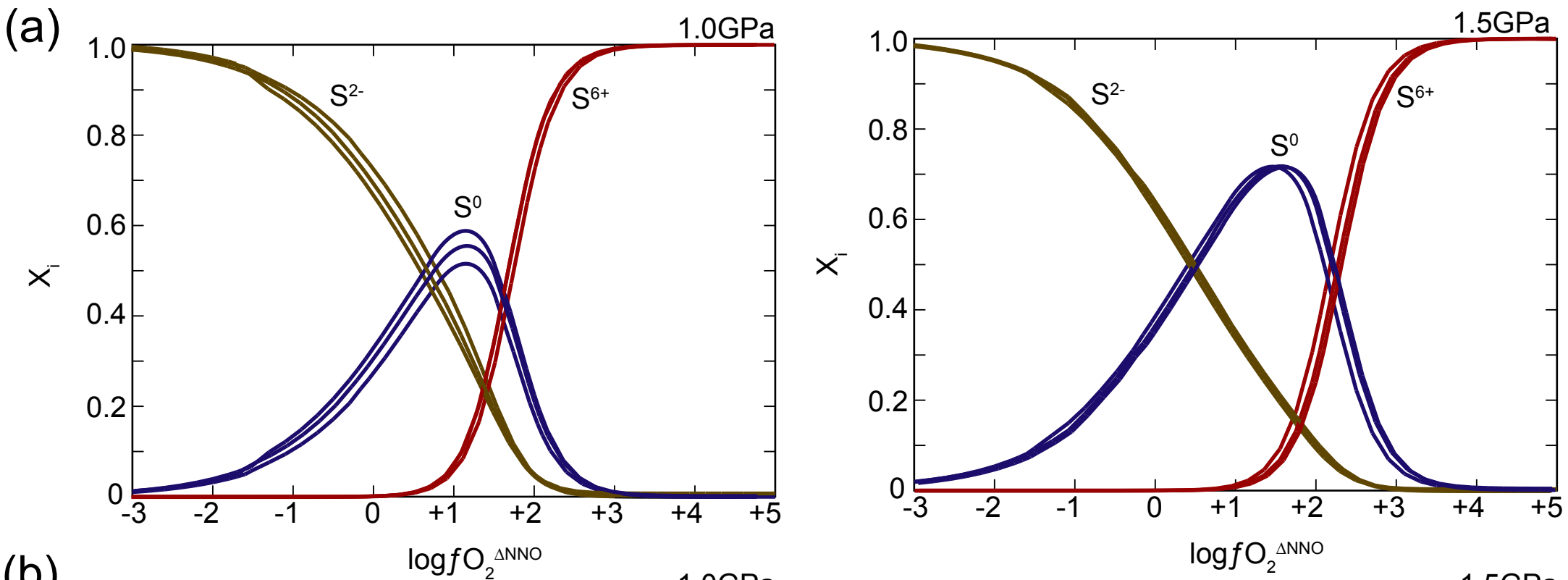
1.0GPa: ○ NNO+4.75 ◇ NNO+2 □ NNO △ NNO-1.5

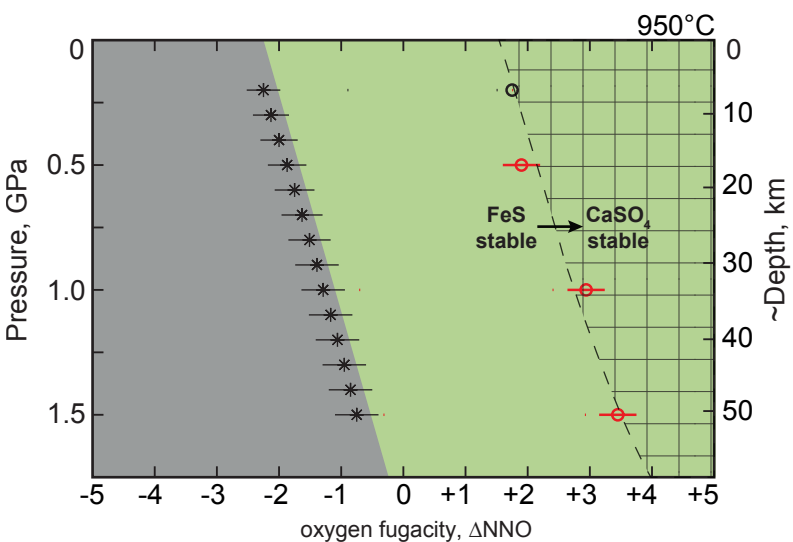
1.5GPa: ◆ NNO+2 ■ NNO ▲ NNO-1.5


★ Starting composition




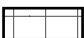






 graphite saturated fluids
no Cu/Au-enrichement

 Cu-enrichment
in fluid saturated melts

 Cu-enrichment
in fluid saturated
and dry melts

Experimental data:



- * graphite-COH fluid equilibrium
Ulmer and Luth (1991)
-  entrance of "sulphate only"
stability field this study
-  entrance of "sulphate only"
stability field
Botcharnikov et al. (2011)

Figure S1: Composition of silicate melts in experiments performed at 1.0 and 1.5GPa. The values are calculated on anhydrous melt basis and represent mean values of 7-21 analyses; error bars refer to $\pm 1\sigma$ reproducibility.

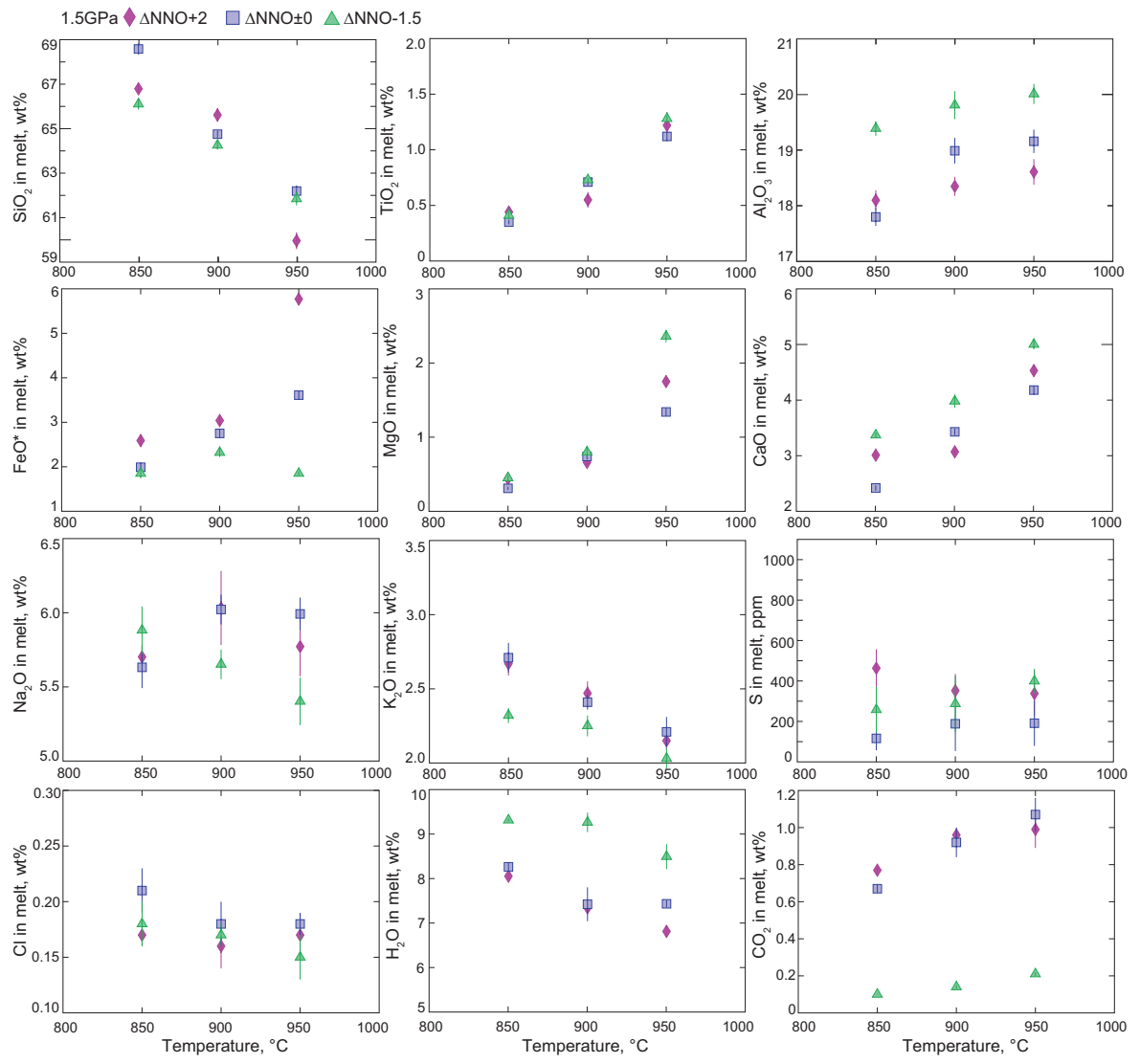


Figure S2: Calculated values for K_A and K_B constants at 1.0 and 1.5GPa. Whilst K_B mostly controls the position of $X_{S^{6+}}$, K_A determines the position of $X_{S^{2-}}$ and X_{S_3} -lines.

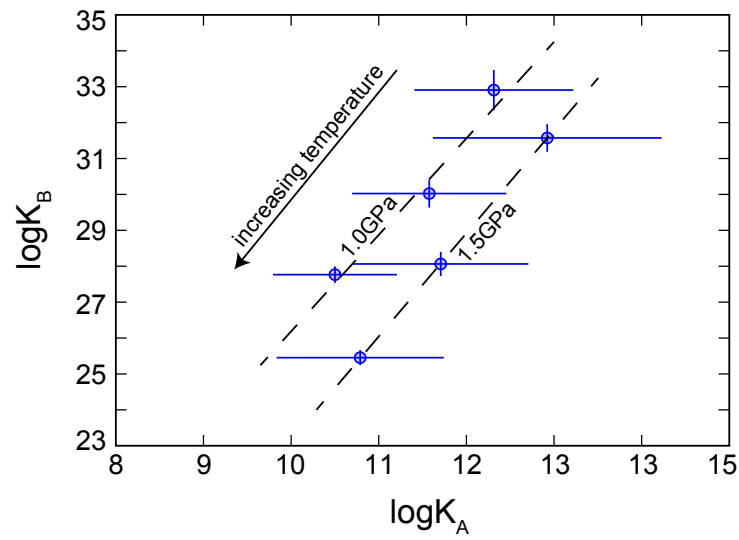


Figure S3: Alternative model to Fig. 8, with (a) S-speciation and (b) S-contents in silicate melts at 1.0 GPa assuming the presence of S^{4+} -intermediate species instead of S^0 . Note the maximum for S^{4+} is closer to the oxidized field compared to S^0 (Fig.8). This would limit the stability field of S^{2-} to below NNO +1 which contradicts the experimental observations.

